Modeling interactions between hydrogen-like atoms and intense laser pulses with the Dirac equation

Andreas Skeidsvoll

Thesis for the degree of Master of Science

Department of Physics and Technology
University of Bergen

May 2018

Acknowledgements

First, I would like to express my greatest gratitude to Prof. Morten Førre for supervising my Master's thesis in an excellent manner. His enthusiasm, insight and ability for explaining complex concepts in an easy manner has been invaluable to the progress of this thesis. I am also very grateful to the rest of the atomic physicists at the University of Bergen, especially for the useful discussions we had in the group meetings at the start of my Master's degree. I would also like to express treat thanks to my fellow students Morten, Markus and Ingunn, for stimulating discussions, the willingness to compare results, and otherwise great times during the past two years.

I am also very grateful to my friends and family, especially to my parents Jarle and Anne Cecilie, my siblings, my roommates in Jonas Reins gate 20, and to a very (very) good friend. Thank you for all the good times we have had, and for all the support you have given me, throughout my Master's degree.

Abstract

In this thesis, a model to describe the interactions between hydrogen-like atoms and intense laser pulses using the Dirac equation is developed. The modeling of these interactions can be motivated by the advances in laser technology through the last decades, which have increased the peak intensities of laser pulses by many orders of magnitude. Improved understanding of how the pulses from the new lasers affect hydrogen-like atoms might transmit to improved understanding of, and control over, various states of matter exposed to intense electromagnetic radiation.

The Dirac equation for the isolated hydrogen-like atom, before interacting with the laser pulse, was solved numerically through the expansion of the solution in both the *dual kinetic balance* basis set and in the *ideal basis set*. Both basis sets were based on B-splines. The ideal basis set was chosen as the preferred one, since the solutions from the dual kinetic basis set displayed an oscillatory behavior at the boundary of the domain. A small relativistic shift in the bound states and in the positive continuum was identified.

The interaction matrix between the hydrogen-like atom and the laser pulse was then calculated by expanding the time dependent solution of the system in the eigenstates of the hydrogen-like atom. This was done both in the dipole approximation, and in an approximation that goes beyond the dipole approximation.

The effect of the interaction with the laser pulse was calculated for both laser pulse approximations using a short-time propagator with the Lanczos algorithm. The total and energy differential photoionization probabilities were then calculated, and compared with results from the Schrödinger equation with and without relativistic corrections. A relativistic shift in both the total photoionization probability and in the locations of the peaks in the energy differential probability plot for the dipole approximation was identified. The transmission to the negative energy continuum states during the time of propagation was shown to be the primary cause of the relativistic effects in the model.

Contents

Chapter 1

Introduction

For centuries, scientists have been trying to understand the nature of light and matter, and how they affect each other. In present times, several reasons for continuing this pursuit can be given. First, new knowledge gained can give us a better idea of the how the universe works, which in itself may be regarded as a desirable outcome. Second, the knowledge may be used to develop technologies that can aid in solving global challenges.

One of the key concepts in natural sciences is that a better understanding of the behavior of the smaller constituents of a physical object can give us a better understanding of the whole. This concept is one of the motivations for doing theoretical and experimental studies on the building blocks of nature, since the understanding gained might translate to a better understanding of the behavior of larger objects.

1.1 The concept of the atom

Already in the ancient Greece, philosophers used philosophical reasoning to come up with the idea that the matter that we surround ourselves with is composed of fundamental and indivisible objects, which they called *atomos* [1]. The theory was a purely philosophical one, as there was no way of experimentally verifying it at the time.

In modern times, the idea of the *atomos* has been revisited, this time in better accord with the scientific method. This modern theory is often accredited to the work done by the chemist John Dalton at the beginning of the nineteenth century. In his work, Dalton proposed that all elements should be composed of extremely small and identical particles, atoms, and he made a system for calculating the weights of these particles from chemical data [2]. Later, Niels Bohr proposed a model for the structure of these atoms, in which they are described as consisting of a positively charged atomic nucleus surrounded by negatively charged electrons, bound together by their mutual electrostatic (Coulomb) attraction [3]. The model postulates that the electrons are confined to move in orbits at a discrete set of distances away from the nucleus, and that the only way to jump between these orbitals is by absorbing or emitting light. This model gave a pretty good explanation of the absorption and emission spectra for hydrogen-like atoms, but failed to explain the spectra for atoms with more than one electron. In hindsight, we can say that the concepts in the Bohr model misrepresented reality; science needed a new theory of the atom.

The conceptual understanding of atoms was stood on its head when the atom was depicted through the theory of *quantum mechanics*. One of the main tools used for modeling the behavior of a quantum mechanical particle is the *Schrödinger equation*, proposed by Erwin Schrödinger [4], which for a free massive particle, and in atomic units, can be written as

$$i\frac{\partial\psi(\mathbf{x},t)}{\partial t} = -\frac{1}{2m}\nabla^2\psi(\mathbf{x},t). \tag{1.1}$$

When modeling the structure of atoms with the Schrödinger equation, the behavior of the the electron is described by the equation, while the atomic nucleus is often assumed to be stationary because of its high mass relative to the mass of the electron. The Coulomb attraction that the electron has to the nucleus can then be introduced into the equation (1.1) by making mathematical substitutions. The effect of other entities that we want to introduce into the system, such as external electromagnetic radiation, can also be introduced through mathematical substitutions.

In the Schrödinger equation, the mathematical description of the state of a system is given by a *wavefunction*, which for the state of electrons in an atom take the shape of *orbitals*. Orbitals are conceptually different from classical elliptic orbits in that they give the probability of observing an electron anywhere in space, instead of giving the definite positions of the electron. The treatment by the Schrödinger equation gave results that agreed better with the experimentally measured properties of atoms than the results from the Bohr model.

1.2 The concept of light

Christian Huygens is often regarded as one of the first proponents of the idea that light behaves like waves [5]. James Clerk Maxwell gave a justification of this wave behavior by treating light as oscillations in the electric and magnetic fields propagating at the speed of light, c [6]. Since non-zero electric and magnetic fields exert forces on charged objects, light incident on atoms may interact with their electrons and change the state of the system.

The electric and magnetic fields can be given a unified mathematical representation through the definition of an electromagnetic scalar potential Φ and an electromagnetic vector potential $\mathbf{A}$, which in atomic units are related to the electric and magnetic fields through

$$\mathbf{E} = -\boldsymbol{\nabla}\phi - \frac{\partial\mathbf{A}}{\partial t}, \tag{1.2}$$

$$\mathbf{B} = \boldsymbol{\nabla}\times\mathbf{A}, \tag{1.3}$$

where $\mathbf{E}$ is the electric field and $\mathbf{B}$ is the magnetic field. These electromagnetic potentials will be used to mathematically represent light in the remainder of this thesis.

1.3 Interactions between atoms and intense laser light

A significant branch of the research on light-matter interactions is concerned with interactions between atoms and intense laser pulses. When the electrons in atoms interact with the oscillating electromagnetic field in an intense laser pulse, they start moving back and forth in space, or *quivering* [7]. This quivering causes the electrons to display "exotic" dynamics, such as peaks in the energy spectrum of the ionized electrons, separated by the energy of the photons in the laser pulse [8]. The research done on the dynamics of these electrons can be seen in context with the advances in laser technology through the last decades, which have increased the obtainable peak intensities of laser pulses by several orders of magnitude. Modern lasers are now able to make electrons quiver with velocities that approach the speed of light relative to the nucleus [9]. These high velocities motivate the use of Albert Einstein's *special theory of relativity* to describe the motion of the electrons, since the Newtonian description breaks down at these velocities [10]. The Schrödinger equation (1.1) is not built on the special theory of relativity in its original form, and hence other equations should be used if the objective is to get an accurate description of interactions between hydrogen-like atoms and these intense laser pulses.

1.4 Aim and approach

In this thesis, we will approach the problem of developing a model for interactions between a hydrogen-like atom and intense laser pulses. The model will treat the electron in the hydrogen-like atom both relativistically and quantum mechanically through the use of the *Dirac equation* proposed by Paul Dirac [11], which for a free particle, and in atomic units, can be written as

$$i\frac{\partial\psi(\mathbf{x},t)}{\partial t} = \left[c\boldsymbol{\alpha}\cdot\mathbf{p} + mc^2\beta\right]\psi(\mathbf{x},t). \tag{1.4}$$

This equation can be understood as a relativistic alternative to the Schrödinger equation. Since the equation incorporates relativistic effects, it will give a better representation of systems where relativistic effects are significant. In the Dirac equation, the state of the system is represented by a multicomponent function known as a *spinor*. Although spinors and Schrödinger wavefunctions have different mathematical properties, they correspond to similar observable physical quantities in systems where relativistic effects are negligible.

A fundamental assumption of our model will be that the interaction between the hydrogen-like atom and the laser pulse happens in empty space, without any external influences. The conventional way of mathematically representing empty space is as a continuous mathematical space that extends infinitely in all directions. For the solution of a differential equation, like the Schrödinger or Dirac equations, to be regarded as *exact* in this space, it has to satisfy the differential equation at each of the infinitely many points in the space. One approach to finding an exact solution of the differential equation is through looking for a solution that is *analytic*. An analytic solution can be written in terms of known functions and can also be verified to be a correct solution. Unfortunately, very few model systems are known to have analytic solutions.

In most of the cases where an analytic solution cannot be found, a *numerical approximation* to the exact solution can still be made. In our model, we will find the numerical solution of the Dirac equation for the isolated hydrogen-like atom by writing the solution as a finite sum of known functions, evaluated at discrete points in a space with finite extent. This method reduces the continuous problem to a discrete problem that can be solved by the use of numerical methods. The way that the equation will be discretized will be discussed in detail in the next chapter.

Modeling of interactions between hydrogen-like atoms and intense laser pulses using the Dirac equation has been attempted multiple times in recent literature [12–18]. This literature refers to several obstacles to the numerical solution of the Dirac equation, such as the appearance of states that do not correlate with any physical quantities, known as *spurious states*. Different methods for overcoming these obstacles have also been described in the literature, such as methods concerning the choice of basis functions and boundary conditions used in the numerical solution. A comparison between some of these methods is done in this thesis, and the most promising method will be implemented in our model.

In the following chapters, we will start by discussing the general properties of the Dirac equation. The Coulomb and external laser potential will be introduced into the Dirac equation through a process called *minimal coupling*. The Dirac equation for the hydrogen-like atom will then be written in a convenient form that exploits the symmetries in our system, in particular by expressing the equation in spherical coordinates.

The process of solving the Dirac equation for the model system will then be split into two parts. First, the Dirac equation for the hydrogen-like atom before the interaction with the laser pulse will be treated. This equation will be solved by converting it into a discrete problem, which will be solved using numerical methods. Second, the interaction that the laser pulse has on the hydrogen-like atom will be treated. This will be done by expressing the whole system in the basis of the solution states obtained in the first part. A numerical propagator will then be used to model how the hydrogen-like atom and laser pulse interact through time.

Finally, we will discuss the results from these solutions. The results will be compared with results from the Schrödinger equation to determine if the Dirac equation reveals relativistic behaviors in hydrogen-like atoms subject to high intensity laser pulses.

1.5 Units

Table 1.1: Atomic units, obtained from [19]. Atomic unit of angular frequency in SI units derived from $\omega = \frac{E}{\hbar}$, and of vector potential derived from $A \propto \frac{E_0}{\omega}$.

Unit	Symbol	Value in SI units
Electron mass	m_e	$9.10938356 \times 10^{-31}$ kg
Elementary charge	e	$1.6021766208 \times 10^{-19}$ C
Reduced Planck's constant	$\hbar = \frac{h}{2\pi}$	$1.054571800 \times 10^{-34}$ Js
Bohr radius	a_0	$5.2917721067 \times 10^{-11}$ m
Hartree energy	E_h	$4.359744650 \times 10^{-18}$ J
Atomic unit of time		$2.418884326509 \times 10^{-17}$ s
Atomic unit of angular frequency		$4.134137334 \times 10^{16}$ s^{-1}
Atomic unit of velocity		$2.18769126277 \times 10^{6}$ ms^{-1}
Atomic unit of electric field		$5.142206707 \times 10^{11}$ Vm^{-1}
Atomic unit of vector potential		$1.243840321 \times 10^{-5}$ Vsm^{-1}

1.6 Conventions

Mathematical operation	Effect
Hermitian conjugate of a matrix or vector	$(\mathbf{A}^\dagger)_{ij} = (\mathbf{A})^*_{ji}$ $\begin{pmatrix} a & b \\ c & d \end{pmatrix}^\dagger = \begin{pmatrix} a^* & c^* \\ b^* & d^* \end{pmatrix}, \quad \begin{pmatrix} a \\ b \end{pmatrix}^\dagger = \begin{pmatrix} a^* & b^* \end{pmatrix}$
Mathematical object	**Definition**
Inner product of functions	$\langle A(x) \vert B(x) \rangle := \int_\Omega A^*(x) B(x)\, \mathrm{d}x$
Inner product of vectors	$\langle \mathbf{A} \vert \mathbf{B} \rangle := \mathbf{A}^\dagger \mathbf{B}$
Anticommutator	$\{A, B\} := AB + BA$
Hermitian matrix	$\mathbf{A}$ such that $\mathbf{A}^\dagger = \mathbf{A}$
n-dimensional identity matrix	$I_n := \begin{pmatrix} 1 & 0 & \dots & 0 \\ 0 & 1 & \dots & 0 \\ \vdots & \vdots & \ddots & \vdots \\ 0 & 0 & \dots & 1 \end{pmatrix}_{n \times n}$
Kronecker delta	$\delta_{ij} := (I_n)_{ij} = \begin{cases} 1, & i = j \\ 0, & \text{otherwise} \end{cases}$
Pauli matrices	$\sigma_x := \begin{pmatrix} 0 & 1 \\ 1 & 0 \end{pmatrix}, \sigma_y := \begin{pmatrix} 0 & -i \\ i & 0 \end{pmatrix}, \sigma_z := \begin{pmatrix} 1 & 0 \\ 0 & -1 \end{pmatrix}$

Chapter 2

Theory and methods

2.1 Prerequisites

2.1.1 Atomic units

Throughout this thesis, *atomic units* will be used. The system of atomic units can be defined by the atomic unit of mass (the electron mass), the atomic unit of charge (the elementary charge), the reduced Planck's constant and the atomic unit of length (the Bohr radius), which are all set to unity in the system. All other units, such as the atomic unit of energy (Hartree, Ha), are derived from these four units using fundamental physical relations. The atomic units relevant to this thesis, together with their value in SI units, can be found in Table 1.1. The value used for the dimensionless fine structure constant is $\alpha = 7.2973525664 \times 10^{-3}$, obtained from [19]. The speed of light in the atomic unit system is $c = \alpha^{-1} \approx 137$ a.u. of velocity.

2.1.2 Relativistic quantum mechanics

The motivation for using the Dirac equation instead of the Schrödinger equation for describing the quantum mechanical behavior of particles at high velocities comes from the theory of special relativity. In nonrelativistic (Newtonian) mechanics, the energy of a classical (not quantum mechanical) free particle is given by

$$E = \frac{\mathbf{p}^2}{2m}, \tag{2.1}$$

where $\mathbf{p}$ is the momentum and m is the mass of the particle. This equation can be quantized by inserting the quantum mechanical *operators* representing the energy and momentum,

$$E = i\frac{\partial}{\partial t}, \quad \mathbf{p} = -i\boldsymbol{\nabla}, \tag{2.2}$$

into the equation, and letting both sides of the equation act on the *wavefunction* $\psi(\mathbf{x}, t)$ from the left. The obtained equation is then the Schrödinger equation

$$i\frac{\partial \psi(\mathbf{x}, t)}{\partial t} = -\frac{1}{2m}\nabla^2 \psi(\mathbf{x}, t). \tag{2.3}$$

From the Schrödinger equation solution $\psi(\mathbf{x}, t)$, a non-negative scalar,

$$\rho = \psi(\mathbf{x}, t)^* \psi(\mathbf{x}, t), \tag{2.4}$$

can be created. This scalar is interpreted as the *probability density* of the particle at the point $(\mathbf{x}, t)$, that is [20],

$$\rho(\mathbf{x}, t)\, \mathrm{d}\mathbf{x} = \left\{ \begin{matrix} \text{probability of finding particle} \\ \text{between } \mathbf{x} \text{ and } \mathbf{x} + \mathrm{d}\mathbf{x}\text{, at time } t \end{matrix} \right\}. \tag{2.5}$$

In relativistic mechanics, the energy of a classical particle is given by a different equation,

$$E^2 = m^2 c^4 + \mathbf{p}^2 c^2. \tag{2.6}$$

Taking the positive square root of this equation, we get

$$E = mc^2 \sqrt{1 + \frac{\mathbf{p}^2}{m^2 c^2}}. \tag{2.7}$$

By Taylor expanding $\sqrt{1 + \frac{\mathbf{p}^2}{m^2 c^2}}$, this equation can be written as

$$E = mc^2 \left[1 + \frac{\mathbf{p}^2}{2m^2 c^2} + \frac{\mathbf{p}^4}{8m^4 c^4} + \dots \right]. \tag{2.8}$$

The first term in the Taylor expansion,

$$E_0 = mc^2, \tag{2.9}$$

is independent of the momentum of the particle, and corresponds to the energy of the particle at rest. This *rest energy* can be subtracted from relativistic energies when comparing them with nonrelativistic energies, since nonrelativistic equations usually do not include the rest energy of the particle. The second term in the expansion in (2.8),

$$E_1 = \frac{\mathbf{p}^2}{2m}, \tag{2.10}$$

is identical to the nonrelativistic energy in (2.1). The terms beyond E_1, like

$$E_2 = \frac{\mathbf{p}^4}{8m^3 c^2}, \tag{2.11}$$

do not have counterparts in nonrelativistic mechanics. Hence, these terms give *relativistic corrections* to the energy in (2.1). Since $\mathbf{p} = m\mathbf{v}$, where $\mathbf{v}$ is the velocity of the particle, the corrections from the terms in (2.8) have increasing powers of $\frac{\mathbf{v}^2}{c^2}$, and hence the later terms only become significant when the velocity v approaches the speed of light c. Since the classical energy of a particle with high velocity gets corrected when transitioning from nonrelativistic to relativistic mechanics, we can also expect the quantized versions of the energy equations to get corrected.

Quantization of the relativistic equation can be done in several ways. One is to quantize a finite number of the terms in the Taylor expanded equation in (2.8) with the

rest energy removed, and effectively obtaining a *semi-relativistic Schrödinger equation*. Another way is to look for a *full-relativistic* alternative equation that incorporates all the terms in the expansion.

One approach to finding the full-relativistic equation is by inserting the operators in (2.2) into the squared energy equation (2.6), giving

$$\left[\frac{\partial^2}{\partial t^2} - c^2\nabla^2 + m^2c^4\right]\phi(\mathbf{x},t) = 0. \tag{2.12}$$

This equation is known as the *Klein-Gordon equation*, and, contrary to the Schrödinger equation, has a time derivative of second order. The density of the Klein-Gordon equation is given by the scalar

$$\rho = \frac{i}{2mc}\left[\phi(\mathbf{x},t)^*\frac{\partial\phi(\mathbf{x},t)}{\partial t} - \frac{\partial\phi(\mathbf{x},t)^*}{\partial t}\phi(\mathbf{x},t)\right], \tag{2.13}$$

which, contrary to the Schrödinger probability density, is not positive definite. Hence, the density can hardly represent a probability density, which was a major obstacle to the acceptance of the Klein-Gordon equation when it was first introduced [21]. The possibility for the density to be negative is caused by the time derivative being of second order.

A new quantum mechanical equation, the *Dirac equation*, grew out of a search for a relativistic equation with a time derivative of first order.

2.1.3 Dirac equation

The Dirac equation, in atomic units, is given by [11]

$$i\frac{\partial\psi(\mathbf{x},t)}{\partial t} = \left[c\boldsymbol{\alpha}\cdot\mathbf{p} + mc^2\beta\right]\psi(\mathbf{x},t), \tag{2.14}$$

where the solutions $\psi(\mathbf{x},t)$ are known as *spinors*. For reasons that will be presented shortly, the Dirac equation is an equation with several components. In order for the Dirac equation to give a valid description of relativistic particles, each component of the spinors should satisfy the Klein-Gordon equation [22]. This can be shown to be the case by moving all terms in the Dirac equation to the left hand side,

$$\left[i\frac{\partial}{\partial t} - c\boldsymbol{\alpha}\cdot\mathbf{p} - mc^2\beta\right]\psi(\mathbf{x},t) = 0, \tag{2.15}$$

and acting on the equation from the left by,

$$-i\frac{\partial}{\partial t} - c\boldsymbol{\alpha}\cdot\mathbf{p} - mc^2\beta. \tag{2.16}$$

Then, inserting $\mathbf{p} = -i\boldsymbol{\nabla}$, we obtain the n-component Klein-Gordon equation,

$$\left[\frac{\partial^2}{\partial t^2} - c^2\nabla^2 + m^2c^4\right]I_n\psi(\mathbf{x},t) = 0, \tag{2.17}$$

as long as α_i and β are n-dimensional matrices satisfying the following conditions

$$\{\alpha_i, \alpha_j\} = 2\delta_{i,j} I_n, \quad \{\alpha_i, \beta\} = 0, \quad \beta^2 = I_n, \tag{2.18}$$

where $i, j \in \{1, 2, 3\}$. In addition, the Dirac equation should also satisfy the continuity equation

$$\frac{\partial \rho}{\partial t} + \boldsymbol{\nabla} \cdot \mathbf{j}, \tag{2.19}$$

with

$$\rho = \psi^\dagger(\mathbf{x}, t)\psi(\mathbf{x}, t), \quad \mathbf{j} = \psi^\dagger(\mathbf{x}, t)\boldsymbol{\alpha}\psi(\mathbf{x}, t), \tag{2.20}$$

which gives the condition that the matrices α_i and β should be Hermitian. For more details, see [21, 22]. All these conditions can be satisfied by letting α_i and β be certain matrices with a dimension of at least four. The representation of the matrices that will be used in this thesis is four-dimensional, and is given by

$$\alpha_i = \begin{pmatrix} 0 & \sigma_i \\ \sigma_i & 0 \end{pmatrix}, \quad \beta = \begin{pmatrix} I_2 & 0 \\ 0 & -I_2 \end{pmatrix}, \tag{2.21}$$

where σ_i are the Pauli matrices and I_2 is the 2-dimensional identity matrix. Using this four-dimensional representation of the α and β-matrices, the spinor $\psi(\mathbf{x}, t)$ in the Dirac equation will be a four component complex function.

2.1.4 Interpretation of the Dirac equation

In quantum mechanics, we interpret the spinor as a function describing the *state* of a spin-1/2 particle, like an electron. The scalar ρ from (2.20) plays the same role as in the Schrödinger equation; it can be interpreted as the probability density of the particle (2.5). Quantum mechanical *obervables*, like the *position*, *momentum* or *energy* of the particle, are represented by Hermitian linear *operators*.

These operators yield real *eigenvalues* when acting on *eigenfunctions* of the operator, which can be illustrated through the *eigenvalue equation* for an operator D,

$$Df = \lambda f, \tag{2.22}$$

where f is the eigenfunction and λ is the eigenvalue of the operator.

Assuming that the state of the system is an *eigenstate* of the operator, its eigenvalue will be the value of the observable in the system. As an example, one can consider the *Hamiltonian* operator H, which is the operator representing the energy of the system. Assuming that the system is the eigenstate $\psi_n(\mathbf{x}, t)$ with energy E_n, the Hamiltonian eigenvalue equation can be written as

$$H\psi_n(\mathbf{x}, t) = E_n\psi_n(\mathbf{x}, t). \tag{2.23}$$

The system can also be in a state that does not have a determined value of the observable, but that can be represented by a *linear combination* of the eigenstates,

$$\Psi(\mathbf{x}, t) = \sum_n c_n\psi_n(\mathbf{x}, t). \tag{2.24}$$

The observed value of such a system will then be the eigenvalue of one of the eigenstates $\psi_n(\mathbf{x}, t)$, with a *probability* given by the square of the coefficient c_n. After observation, the state of the system will then be in the eigenstate $\psi_n(\mathbf{x}, t)$. We say that through this process, the state of the system has *collapsed* to one of the eigenstates.

2.1.5 Setting up a matrix eigenvalue problem

A numerical approximation to the solution of a general eigenvalue problem like (2.22) can be found by the method outlined in this section. First, one starts by expanding the eigenfunction f in a set of linearly independent basis functions with corresponding unknown coefficients,

$$f = \sum_{j=1}^{N} v_j F_j, \tag{2.25}$$

where the F_j are the basis functions and the v_j are the coefficients. Inserting this expanded solution into the general eigenvalue problem in (2.22), one obtains

$$D \sum_{j=1}^{N} v_j F_j = \lambda \sum_{i=1}^{N} v_j F_j. \tag{2.26}$$

Multiplying this equation from the left by an arbitrary basis function in the basis set, F_i and integrating over the domain of the basis functions, effectively doing an inner product, one obtains the equation

$$\sum_{j=1}^{N} \langle F_i | \, D \, | F_j \rangle \, v_j = \lambda \sum_{j=1}^{N} \langle F_i | F_j \rangle \, v_j. \tag{2.27}$$

If one defines the matrix $\mathbf{D}$ with elements

$$(\mathbf{D})_{ij} = \langle F_i | \, D \, | F_j \rangle, \tag{2.28}$$

and the matrix $\mathbf{S}$, also known as the *overlap matrix*, with elements

$$(\mathbf{S})_{ij} = \langle F_i | F_j \rangle, \tag{2.29}$$

the equation (2.27) can be written as a $N \times N$ generalized matrix eigenvalue problem

$$\mathbf{D}\mathbf{v} = \lambda \mathbf{S}\mathbf{v}. \tag{2.30}$$

The vector of coefficients $\mathbf{v}$ is also known as the *eigenvector* of the matrix eigenvalue problem, and is given by

$$\mathbf{v} = \begin{pmatrix} v_1 \\ v_2 \\ \vdots \\ v_N \end{pmatrix}. \tag{2.31}$$

The eigenvalue problem in (2.30) can be solved for a set of these eigenvectors with corresponding eigenvalues λ, using numerical methods found in many numerical libraries. The number of solutions of the eigenvalue problem is N, which is the same as the number of linearly independent functions in the basis set.

2.2 The modeled system

2.2.1 Minimal coupling

The Dirac equation, as stated in (2.14), describes the motion of a single free particle with spin 1/2. This model of the free particle can be used as a starting point for describing more complex physical systems, like systems where the particle is subject to forces. The more complex systems can be modeled by making changes to the Dirac equation that mathematically represent the different entities that one wants to introduce into the free electron system.

In this thesis, the spin 1/2 particle that will be modeled with the Dirac equation is the electron. Two different physical entities will be introduced into the free electron system: a positive point charge, which represents a hydrogen-like nucleus, and a laser pulse. We assume that the different entities in the new system only interact through the *electromagnetic force*, and that the hydrogen-like nucleus is so heavy that the effects of the electromagnetic forces on it are negligible. The interactions between the different entities in the system will be treated within the *first quantization* treatment of quantum mechanics, which means the number of particles in the system will be conserved under interaction. This is done by letting all objects except for the electron be represented by classical potentials. Since the electron is treated quantum mechanically and the other entities treated classically, this is also known as a *semi-classical* treatment.

The classical potentials will be introduced into the free particle system using a procedure called *minimal coupling*, which is valid as long as all charges in the system are assumed to be point charges.

In minimal coupling, we make the substitutions [21]

$$i\frac{\partial}{\partial t} \rightarrow i\frac{\partial}{\partial t} - q\Phi(\mathbf{x}, t), \tag{2.32}$$

where Φ is the scalar electromagnetic potential, and

$$\mathbf{p} \rightarrow \mathbf{p} - q\mathbf{A}(\mathbf{x}, t) \tag{2.33}$$

where $\mathbf{A}(\mathbf{x}, t)$ is the vector electromagnetic potential, and where q is the charge of the considered particle. The minimally coupled Dirac equation from (2.14) will then take the form

$$i\frac{\partial\psi(\mathbf{x}, t)}{\partial t} = \big(c\boldsymbol{\alpha} \cdot [\mathbf{p} - q\mathbf{A}(\mathbf{x}, t)] + c^2\beta + q\Phi(\mathbf{x}, t)I_4\big)\psi(\mathbf{x}, t). \tag{2.34}$$

For an electron, $q = -e = -1$ a.u. and $m = m_e = 1$ a.u. The attraction to the hydrogen-like nucleus with charge Z will be represented by a scalar Coulomb potential $\Phi = \frac{Z}{r}$, and the effect of the laser pulse will be represented by a time dependent vector potential $\mathbf{A}(\mathbf{x}, t) = \mathbf{A}(\eta)$, where η is a function of $\mathbf{x}$ and t. The Dirac equation for the hydrogen-like atom and laser pulse system will then take the form

$$i\frac{\partial\psi(\mathbf{x}, t)}{\partial t} = \left(c\boldsymbol{\alpha} \cdot [\mathbf{p} + \mathbf{A}(\eta)] + c^2\beta - \frac{Z}{r}I_4\right)\psi(\mathbf{x}, t). \tag{2.35}$$

The operator on the right hand side of the equation is the total Hamiltonian of the system,

$$H(t) = c\boldsymbol{\alpha} \cdot [\mathbf{p} + \mathbf{A}(\eta)] + c^2\beta - \frac{Z}{r}I_4. \tag{2.36}$$

This Hamiltonian will be split into two parts, one part describing the hydrogen-like atom without the interaction with the laser pulse, H_0, and one part describing the time dependent interaction with the laser pulse, $V(t)$,

$$H(t) = H_0 + V(t), \tag{2.37}$$

where

$$H_0 = c\boldsymbol{\alpha} \cdot \mathbf{p} + c^2\beta - \frac{Z}{r}I_4, \tag{2.38}$$

and

$$V(t) = c\boldsymbol{\alpha} \cdot \mathbf{A}(\eta). \tag{2.39}$$

In this thesis, it will be assumed that the laser vector potential does not interact with the system at $t = 0$. Then, $V(0) = 0$, giving

$$H(0) = H_0. \tag{2.40}$$

The solution of the Dirac equation with the Hamiltonian H_0 can then be considered separately, before introducing the interaction with the laser pulse.

2.2.2 Derivation of hydrogen-like radial equation

In this section, we will separate the radial and angular parts of the Dirac equation for the electron in the hydrogen-like atom. The Dirac equation for this system is given by

$$i\frac{\partial\psi(\mathbf{x},t)}{\partial t} = H_0\psi(\mathbf{x},t) = \left[c\boldsymbol{\alpha} \cdot \mathbf{p} + c^2\beta - \frac{Z}{r}I_4\right]\psi(\mathbf{x},t). \tag{2.41}$$

We will look for stationary states of this system of the form

$$\psi(\mathbf{x},t) = e^{-iEt}\phi(\mathbf{x}), \tag{2.42}$$

so that E will be an eigenvalue of the Dirac Hamiltonian H_0 from (2.38),

$$H_0\phi(\mathbf{x}) = E\phi(\mathbf{x}). \tag{2.43}$$

Using the representation (2.21)

$$\boldsymbol{\alpha} = \begin{pmatrix} 0 & \boldsymbol{\sigma} \\ \boldsymbol{\sigma} & 0 \end{pmatrix}, \quad \beta = \begin{pmatrix} I_2 & 0 \\ 0 & -I_2 \end{pmatrix}, \tag{2.44}$$

the hydrogen-like Hamiltonian (2.38) can be written on the form

$$H_0 = \begin{pmatrix} \left[c^2 - \frac{Z}{r}\right]I_2 & c\boldsymbol{\sigma} \cdot \mathbf{p} \\ c\boldsymbol{\sigma} \cdot \mathbf{p} & \left[-c^2 - \frac{Z}{r}\right]I_2 \end{pmatrix}. \tag{2.45}$$

Since the scalar Coulomb potential $\frac{Z}{r}$ is spherically symmetric, it is useful to express the equation 2.43 in spherical coordinates. Following [21][Section 3.2.3], one can rewrite the operator $c\boldsymbol{\sigma} \cdot \mathbf{p}$ in spherical coordinates as

$$c\boldsymbol{\sigma} \cdot \mathbf{p} = -ic\sigma_r\left(\frac{\partial}{\partial r} + \frac{K+1}{r}\right), \tag{2.46}$$

where the operator K is given by

$$K = -(1 + \boldsymbol{\sigma} \cdot \mathbf{l}), \tag{2.47}$$

with the operator l being the angular momentum operator from nonrelativistic quantum mechanics [20],

$$\mathbf{l} = -i(\mathbf{r} \times \boldsymbol{\nabla}). \tag{2.48}$$

The Hamiltonian H_0 does not commute with the operators $\mathbf{l}^2$, $l_z = \hat{\mathbf{z}} \cdot \mathbf{l}$ and $s_z = \frac{1}{2}\boldsymbol{\sigma}$ from nonrelativistic quantum mechanics, and hence the quantum numbers l, m_l and m_s are not good quantum numbers for the states of the hydrogen-like atom in the Dirac equation [21]. A good set of quantum numbers can be found through the eigenvalue equation of the K-operator,

$$K\chi_{\kappa,\mu}(\hat{\mathbf{r}}) = \kappa\chi_{\kappa,\mu}(\hat{\mathbf{r}}). \tag{2.49}$$

In this equation, the two-component function $\chi_{\kappa,\mu}$ is called a *spherical spinor*, with the vector $\hat{\mathbf{r}}(\theta, \varphi)$ giving the position on the unit sphere [23]. For more details on the algebraic derivation of this relation, see for example [24]. The quantum number μ corresponds to the projection of the total angular momentum of the state along the z-axis, and it is an eigenvalue of the j_z-operator from nonrelativistic quantum mechanics,

$$j_z\chi_{\kappa,\mu}(\hat{\mathbf{r}}) = \mu\chi_{\kappa,\mu}(\hat{\mathbf{r}}), \tag{2.50}$$

where

$$j_z = l_z + s_z = -i\left(x\,\frac{\partial}{\partial y} - y\frac{\partial}{\partial x}\right) + \frac{1}{2}\sigma_z. \tag{2.51}$$

The possible values that the two quantum numbers can take on are $\kappa \in \{\pm 1, \pm 2, \ldots\}$ and $\mu \in \{-|\kappa| + \frac{1}{2}, \ldots, |\kappa| - \frac{1}{2}\}$. The spherical spinors $\chi_{\kappa,\mu}$, constitute a complete set of two-component functions defined on the unit sphere [25], which are orthonormal with respect to the inner product [21]

$$\left\langle \chi_{\kappa',\mu'} \middle| \chi_{\kappa,\mu} \right\rangle = \int \chi^{\dagger}_{\kappa',\mu'}(\hat{\mathbf{r}})\chi_{\kappa,\mu}(\hat{\mathbf{r}})\,\mathrm{d}\hat{\mathbf{r}} = \delta_{\kappa',\kappa}\delta_{\mu',\mu}. \tag{2.52}$$

Inserting (2.46) into (2.45), we get that

$$H_0 = \begin{pmatrix} \left[c^2 - \frac{Z}{r}\right] I_2 & -ic\sigma_r\left[\frac{\partial}{\partial r} + \frac{K+1}{r}\right] \\ -ic\sigma_r\left[\frac{\partial}{\partial r} + \frac{K+1}{r}\right] & \left[-c^2 - \frac{Z}{r}\right] I_2 \end{pmatrix}. \tag{2.53}$$

In a spherical coordinate system (r, θ, φ), eigenstates of the Hamiltonian in (2.53) have the 4-spinor structure [21]

$$\phi(\mathbf{x}) = \frac{1}{r}\begin{pmatrix} P(r)\chi_{\kappa,\mu}(\hat{\mathbf{r}}) \\ iQ(r)\chi_{-\kappa,\mu}(\hat{\mathbf{r}}) \end{pmatrix}. \tag{2.54}$$

Since [21]

$$\sigma_r\chi_{\kappa,\mu}(\hat{\mathbf{r}}) = -\chi_{-\kappa,\mu}(\hat{\mathbf{r}}), \tag{2.55}$$

and since

$$\left(\frac{d}{dr} + \frac{1}{r}\right)\frac{f(r)}{r} = \frac{1}{r}\frac{df(r)}{dr}, \tag{2.56}$$

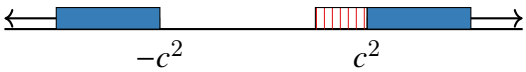

Figure 2.1: Illustration of the analytic spectrum of the Dirac hydrogen-like Hamiltonian. An infinite number of discrete bound states have energies in the region $-c^2 < E < c^2$. The positive and negative continua have energies above c^2 and below $-c^2$, respectively.

(2.43) can be written as

$$\begin{aligned}(H_0 - E)\phi(\mathbf{x}) =& \begin{pmatrix} \left[c^2 - \frac{Z}{r} - E\right] I_2 & -ic\sigma_r\left[\frac{\partial}{\partial r} + \frac{K+1}{r}\right] \\ -ic\sigma_r\left[\frac{\partial}{\partial r} + \frac{K+1}{r}\right] & \left[-c^2 - \frac{Z}{r} - E\right] I_2 \end{pmatrix} \frac{1}{r} \begin{pmatrix} P(r)\chi_{\kappa,\mu}(\hat{\mathbf{r}}) \\ iQ(r)\chi_{-\kappa,\mu}(\hat{\mathbf{r}}) \end{pmatrix} \\ =& \frac{1}{r} \begin{pmatrix} \left[c^2 - \frac{Z}{r} - E\right] P(r)\chi_{\kappa,\mu}(\hat{\mathbf{r}}) + c\sigma_r\left[\frac{\partial}{\partial r} + \frac{\kappa}{r}\right] Q(r)\chi_{-\kappa,\mu}(\hat{\mathbf{r}}) \\ -ic\sigma_r\left[\frac{\partial}{\partial r} + \frac{\kappa}{r}\right] P(r)\chi_{\kappa,\mu}(\hat{\mathbf{r}}) + i\left[-c^2 - \frac{Z}{r} - E\right] Q(r)\chi_{-\kappa,\mu}(\hat{\mathbf{r}}) \end{pmatrix} \\ =& \frac{1}{r} \begin{pmatrix} \left(\left[c^2 - \frac{Z}{r} - E\right] P(r) + c\left[\frac{\kappa}{r} - \frac{\partial}{\partial r}\right] Q(r)\right)\chi_{\kappa,\mu}(\hat{\mathbf{r}}) \\ i\left(c\left[\frac{\kappa}{r} + \frac{\partial}{\partial r}\right] P(r) + \left[-c^2 - \frac{Z}{r} - E\right] Q(r)\right)\chi_{-\kappa,\mu}(\hat{\mathbf{r}}) \end{pmatrix} \\ =& 0. \end{aligned} \tag{2.57}$$

Non-zero factors can be removed from (2.57), and the equation can thus be written on the two-component form

$$\begin{pmatrix} c^2 - \frac{Z}{r} & c\left[\frac{\kappa}{r} - \frac{d}{dr}\right] \\ c\left[\frac{\kappa}{r} + \frac{d}{dr}\right] & -c^2 - \frac{Z}{r} \end{pmatrix} \begin{pmatrix} P(r) \\ Q(r) \end{pmatrix} = E \begin{pmatrix} P(r) \\ Q(r) \end{pmatrix} = H_0 \begin{pmatrix} P(r) \\ Q(r) \end{pmatrix}. \tag{2.58}$$

As we can see, we were able to separate out the angular dependency of the hydrogen-like Dirac equation by introducing the quantum number κ. The equation (2.58) is a system of two coupled first order differential equations in only one variable; the radial variable r. This equation will hereafter be referred to as the *hydrogen-like radial equation*. The hydrogen-like radial equation was solved numerically on finite domains $r \in [a, b]$, using the method described in Section 2.3.

2.2.3 Dirac hydrogen-like spectrum

The Dirac equation allows solutions with negative energy. An illustration of the form of the analytic spectrum of the Dirac hydrogen-like Hamiltonian on the domain $r \in [0, \infty]$ is shown in Figure 2.1. As we can see, the hydrogen-like spectrum has a positive energy continuum for $E > c^2$ and a negative energy continuum for $E < -c^2$. Between these continua, discrete *bound states* can be found; states that are confined to the nucleus by the Coulomb potential. The analytic solution of the hydrogen-like radial equation on the domain $r \in [0, \infty)$ is often done in textbooks on relativistic quantum mechanics, and gives the formula for the relativistic hydrogen-like bound state energies [26]

$$E_{n,\kappa} = \frac{c^2}{\sqrt{1 + \frac{Z^2\alpha^2}{\left(n + \sqrt{\kappa^2 - Z^2\alpha^2}\right)^2}}}, \tag{2.59}$$

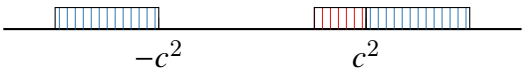

Figure 2.2: Illustration of the spectrum of the Dirac hydrogen-like Hamiltonian on a finite domain and with a finite number of basis functions. A finite number of discrete bound states have energies in the region $-c^2 < E < c^2$. The positive and negative discrete pseudocontinua have energies above c^2 and below $-c^2$, respectively.

where $n \in \{0, 1, \ldots\}$ for positive κ, and $n \in \{1, 2, \ldots\}$ for negative κ.

In this thesis, the Dirac hydrogen-like equation will be numerically solved on a finite domain $r \in [a, b]$, and with a finite number of basis functions. When the domain is finite, the states with energies above c^2 and below $-c^2$ will also be discrete. These states will be referred to as the positive and negative *pseudocontinuum* states. The number of energies in the numerical spectrum is also equal to the number of basis functions used in the calculations, which means the number of energies will be finite in the calculations. An illustration of the finite spectrum is given in Figure 2.2. Theoretically, the Dirac equation does not have a lower bound on the spectrum, but we will refer to the bound state with the lowest energy $E > c^2$ as the *ground state* of the system. The energies in the spectrum for a finite number of basis functions is fortunately centered around $E = 0$, which means we get a good description of the behavior of the system for energies with an absolute value lower than the maximum energy in the spectrum.

2.2.4 Connection to Schrödinger equation states

As we have seen, the Dirac quantum states can be labeled by the three quantum numbers (n, κ, μ). The quantum number κ can be related to the total angular momentum quantum number j through [23]

$$j = |\kappa| - \frac{1}{2}. \tag{2.60}$$

In (2.58) the lower equation can be solved for $Q(r)$, giving

$$Q(r) = \frac{c}{c^2 + E + \frac{Z}{r}} \left[\frac{d}{dr} + \frac{\kappa}{r} \right] P(r). \tag{2.61}$$

Since the relativistic energy E for positive energy states includes the electron's rest energy c^2, it can be written as $E = c^2 + E'$, where E' is the energy without the rest energy. Inserting this relation into (2.61), one obtains

$$Q(r) = \frac{c}{2c^2 + E' + \frac{Z}{r}} \left[\frac{d}{dr} + \frac{\kappa}{r} \right] P(r). \tag{2.62}$$

The nonrelativistic limit of this equation can be found by letting $c \to \infty$, giving

$$Q(r) \approx \frac{1}{2c} \left[\frac{d}{dr} + \frac{\kappa}{r} \right] P(r). \tag{2.63}$$

and $Q(r) \to 0$ for all r. The fact that $Q(r) \to 0$ is the reason that the lower component often is referred to as the *small component* of positive energy spinors. In the nonrelativistic limit, the positive energy spinors behave like the upper component of the spinor

only, which has a definite angular momentum l. The quantum number κ for the spinor can then be related to the nonrelativistic quantum number l through [23]

$$l = \left|\kappa + \frac{1}{2}\right| - \frac{1}{2}. \tag{2.64}$$

From (2.50), it can be seen that the quantum number μ is the same number as the nonrelativistic eigenvalue of the j_z-operator, m_j. More information about the quantum numbers l, j and m_j can be found in textbooks on nonrelativistic quantum mechanics like [20]. Given the relationships above, the Dirac bound states can be labeled by the symbols commonly used for nonrelativistic orbitals,

$$Nl_j, \tag{2.65}$$

where N is the *principal quantum number*

$$N = n + |\kappa|, \tag{2.66}$$

with n from (2.59), and the numerical value of l is exchanged with the letters commonly used in nonrelativistic quantum mechanics $l = s, p, d, f \ldots$. For example, the lowest energy bound state of $\kappa = -1$ can be labeled as the $1s_{1/2}$-state, the lowest energy bound state of $\kappa = 1$ can be labeled as the $2p_{1/2}$-state, and so on.

2.2.5 Pulse geometry

The laser light of extremely intense lasers are emitted in pulses, which in effect only interact with the hydrogen-like atom for a finite amount of time. Mathematically, these pulses can be modeled by choosing a mathematical function that is non-zero only inside a finite region in space and time. We will choose a vector potential commonly used in the literature [13, 27, 28],

$$\mathbf{A}(\eta) = \frac{\mathbf{E}_0}{\omega} \sin^2\left(\frac{\pi\eta}{\omega T}\right) \sin(\eta + \phi), \quad 0 \leq \eta \leq \omega T. \tag{2.67}$$

where $\eta = \omega t - \mathbf{k} \cdot \mathbf{r}$. In this vector potential, the $\sin$-function is the *carrier* of the pulse, which has the *carrier frequency* ω and the *wave vector* $\mathbf{k}$. The carrier is modulated by the $\sin^2$-function, the *envelope* of the pulse, which has the period T. The scalar ϕ is called the carrier-envelope phase, which gives the phase between the carrier and the envelope functions. The vector $\mathbf{E}_0$ is the maximum electric field strength in the direction of polarization. Assuming that the pulse is linearly polarized, giving $\mathbf{E}_0 = E_0\hat{\mathbf{e}}$, where $\hat{\mathbf{e}}$ is the direction of propagation, (2.67) can be written as

$$\begin{aligned}\mathbf{A}(\eta) =& \frac{E_0}{\omega} \sin^2\left(\frac{\pi\eta}{\omega T}\right) \sin(\eta + \phi)\hat{\mathbf{e}}, \quad 0 \leq \eta \leq \omega T \\ =& A(\eta)\hat{\mathbf{e}}.\end{aligned} \tag{2.68}$$

The component $A(\eta)$ of this vector potential satisfies the scalar electromagnetic wave equation

$$\frac{1}{c^2}\frac{\partial^2 A(\eta)}{\partial t^2} - \nabla^2 A(\eta) = 0. \tag{2.69}$$

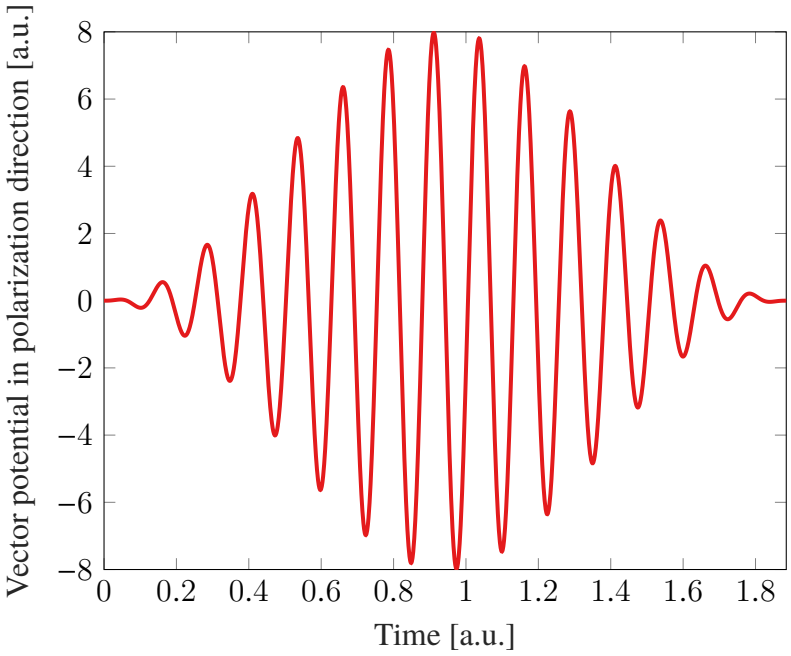

Figure 2.3: Temporal profile of the pulse in (2.68) at $r = 0$. The electric field strength was set to $E_0 = 400$ a.u., the frequency to $\omega = 50$ a.u. and the pulse was chosen to be a 15 cycle pulse, that is $T = 15\frac{2\pi}{\omega}$ a.u.

At the point $r = 0$ a.u., the laser pulse has the temporal profile in the polarization direction shown in Figure 2.3. If we assume that the pulse is x-polarized and propagating in the z-direction, we get

$$\mathbf{k} = \frac{\omega}{c}\hat{\mathbf{z}} \rightarrow \eta = \omega\left(t - \frac{z}{c}\right). \tag{2.70}$$

The equation (2.68) will then take the form

$$\mathbf{A}(\eta) = \frac{E_0}{\omega}\sin^2\left[\frac{\pi}{T}\left(t - \frac{z}{c}\right)\right]\sin\left[\omega\left(t - \frac{z}{c}\right) + \phi\right]\hat{\mathbf{x}}, \quad 0 \leq t - \frac{z}{c} \leq T. \tag{2.71}$$

The full geometry of the pulse given in (2.71) is hard to implement into the numerical methods used for solving the time dependent Dirac equation. Hence, approximations to the pulse geometry is often used.

A commonly used approximation is the *dipole approximation*, which can be made by letting $\eta \rightarrow \omega t$, removing all spatial dependency of the laser pulse except for the direction of polarization. This gives

$$\mathbf{A}(\eta) = \frac{E_0}{\omega}\sin^2\left(\frac{\pi t}{T}\right)\sin(\omega t + \phi)\hat{\mathbf{x}}, \quad 0 \leq t \leq T. \tag{2.72}$$

In addition to treating the laser pulse with the dipole approximation, another approximation to the pulse geometry will be considered in this thesis. In this approximation, hereafter referred to as the *beyond dipole approximation*, the full spatial dependency of the vector potential *function* is retained. The approximation is done only on the *domain* of the time variable t. If no approximation were to be made, the time variable would, from (2.71), be limited by

$$\frac{z}{c} \leq t \leq T + \frac{z}{c}. \tag{2.73}$$

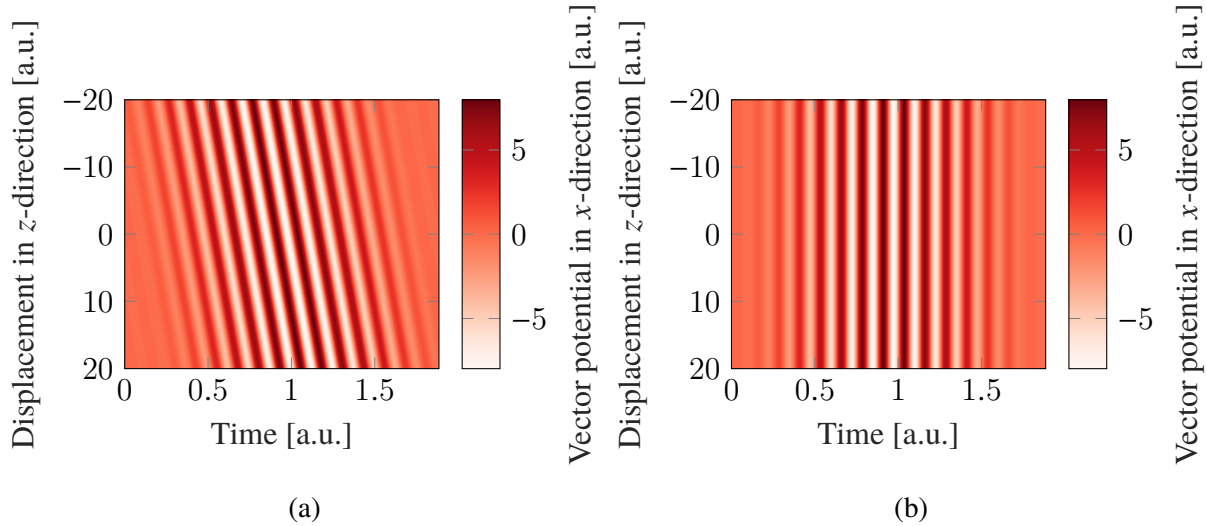

Figure 2.4: The geometry of the laser pulse with (a) the beyond dipole approximation and (b) the dipole approximation. The pulses have the parameters $E_0 = 400$ a.u., $\omega = 50$ a.u. and $T = 15\frac{2\pi}{\omega}$ a.u.

Since the limits for the time variable is z-dependent, the area spanned by t and z will have a skewed boundary. In the beyond dipole approximation, this z-dependency of the boundary is neglected, giving the new limits on the boundary

$$0 < t < T. \tag{2.74}$$

This gives the equation

$$\mathbf{A}(\eta) = \frac{E_0}{\omega} \sin^2\left[\frac{\pi}{T}\left(t - \frac{z}{c}\right)\right] \sin\left[\omega\left(t - \frac{z}{c}\right) + \phi\right]\hat{\mathbf{x}}, \quad 0 \leq t \leq T. \tag{2.75}$$

This approximation has been implemented in a recent article [28], and has shown to be successful for describing the ionization by a pulse with 15 optical cycles, that is $T = 15\frac{2\pi}{\omega}$ a.u.

The beyond dipole approximation will be treated by expanding the vector potential function in spherical harmonics in Section 2.4.1, inspired by [28]. A figure of both the dipole and beyond dipole approximations is shown in Figure 2.4. When solving the time dependent Dirac equation, we will assume that the hydrogen-like atom system is an eigenstate of the time dependent Hamiltonian at $t = 0$ and $t = T$. This assumption will be valid as long as the vector potential is zero at these two times. From (2.72), it can be seen that this is the case for the vector potential in the dipole approximation. The vector potential with the beyond dipole approximation in (2.75), on the hand, is not necessarily zero at $t = 0$ and $t = T$, see the the left panel of Figure 2.4, since the vector potential also has a z-dependency. Nonetheless, since the electron in the ground state is located close to the nucleus, and since the effect of the z-coordinate is scaled by $1/c$, we can assume that the influence of the laser potential is small enough at $t = 0$ and $t = T$ to treat it as if it was zero.

2.3 Numerical solution of Dirac hydrogen-like radial equation

The first goal in the thesis is to solve the radial equation for the hydrogen-like system numerically for any κ. This will be done by expanding the two-component solution of the Dirac hydrogen-like radial equation (2.58) in a finite set of linearly independent basis functions with unknown coefficients, just as is done for a general operator in Section 2.1.5.

2.3.1 Comment on the choice of basis set

The radial Dirac equation (2.58) is a two component equation, and hence the basis functions need to span the space of two component functions. Extra care is needed when choosing the basis functions for solving the radial Dirac equation, since naive choices of basis functions have been shown to give *spurious states* in the solution space [29]. For more detail on the cause of the spurious states, see [30].

Several methods that aim to remove the spurious states have been proposed in the literature, one of the most renowned being the method of dual kinetic balance introduced by Shabaev et. al.[31]. In the dual kinetic balance basis set, the components of the basis functions are related by the same relation that the components of the solution of the radial equation have in the nonrelativistic limit, like in (2.63) for positive energy states. Although the method in practice often removes the spurious states from the spectrum, Lewin and Séré argue that there is no rigorous ground to believe that the method of dual kinetic balance removes all spurious states from the spectrum [30]. In our studies, we have also experienced apparent problems at the boundary of the domain when using the dual kinetic balance basis set, which will be demonstrated in Section 3.1.1. The details of how the dual kinetic basis set is constructed will not be given in this thesis, but can be found in the article by Shabaev et. al.[31].

A different article by Munger gives an alternative remedy to the problem of spurious states, where the Dirac radial hydrogen-like Hamiltonian is transformed by a similarity transformation [32]. The article argues formally that the transformed Hamiltonian operator has a spectrum that converges to the proper spectrum without spurious eigenvalues when the size of the domain and the number of basis functions approach infinity. The solutions of the similarity transformed Hamiltonian can then be transformed back to the usual Dirac solutions by applying the inverse transformation.

2.3.2 Ideal basis set

The procedure for setting up the eigenvalue problem with the ideal basis set is outlined in the following section. For more details, refer to [32].

In [32, Section X], it is argued that two different similarity transformations should be used for the different signs of κ, to avoid missing or added states in the solution space. The operator h, used for positive κ, and the operator $\tilde{h}$, used for negative κ, are found by the similarity transformations

$$h = UH_\alpha U^{-1}, \quad \tilde{h} = \tilde{U}H_\alpha \tilde{U}^{-1}, \tag{2.76}$$

respectively, where H_α is the hydrogen-like radial Hamiltonian H from (2.58) multiplied

by α^2, having the eigenvalues $\epsilon = \alpha^2 E$. The unitary matrices U and $\tilde{U}$ are given by

$$U = \begin{pmatrix} \sqrt{\frac{\kappa-\gamma}{2\kappa}} & \operatorname{sgn}(\kappa)\sqrt{\frac{\kappa+\gamma}{2\kappa}} \\ -\operatorname{sgn}(\kappa)\sqrt{\frac{\kappa+\gamma}{2\kappa}} & \sqrt{\frac{\kappa-\gamma}{2\kappa}} \end{pmatrix}, \quad \tilde{U} = \begin{pmatrix} \sqrt{\frac{\kappa+\gamma}{2\kappa}} & \operatorname{sgn}(\kappa)\sqrt{\frac{\kappa-\gamma}{2\kappa}} \\ -\operatorname{sgn}(\kappa)\sqrt{\frac{\kappa-\gamma}{2\kappa}} & \sqrt{\frac{\kappa+\gamma}{2\kappa}} \end{pmatrix}, \tag{2.77}$$

where

$$\gamma = \sqrt{\kappa^2 - (Z\alpha)^2}. \tag{2.78}$$

Applying these unitary transformations, the operators h and $\tilde{h}$ in (2.76) can be written as

$$h = \begin{pmatrix} \eta(\kappa) & B(\kappa) \\ B^\dagger(\kappa) & -\eta(\kappa) - A \end{pmatrix}, \quad \tilde{h} = \begin{pmatrix} \eta(-\kappa) & -B^\dagger(-\kappa) \\ -B(-\kappa) & -\eta(-\kappa) - A \end{pmatrix}, \tag{2.79}$$

where

$$\eta(\kappa) = -\frac{\gamma}{\kappa}, \quad A = \frac{2Z\alpha^2}{r}, \quad B(\kappa) = -\alpha\left(\frac{Z}{\kappa} + \frac{\gamma}{r} + \frac{d}{dr}\right), \quad B^\dagger(\kappa) = -\alpha\left(\frac{Z}{\kappa} + \frac{\gamma}{r} - \frac{d}{dr}\right). \tag{2.80}$$

The solutions Φ and $\tilde{\Phi}$ of the eigenvalue problems

$$h\Phi = \epsilon\Phi, \quad \tilde{h}\tilde{\Phi} = \epsilon\tilde{\Phi} \tag{2.81}$$

will be expanded in two different basis sets of $2N$ functions,

$$W_k = \begin{pmatrix} B(\kappa)w_k \\ 0 \end{pmatrix}, \quad W_{k+N} = \begin{pmatrix} 0 \\ w_k \end{pmatrix}, \quad \tilde{W}_k = \begin{pmatrix} -B^\dagger(-\kappa)w_k \\ 0 \end{pmatrix}, \quad \tilde{W}_{k+N} = \begin{pmatrix} 0 \\ w_k \end{pmatrix}, \tag{2.82}$$

where $k = 1, \ldots, N$ and the w_k are linearly independent functions forming a basis for the Sobolev space of square integrable functions and first derivatives. The Dirichlet boundary conditions is imposed on the functions, in other words $w_k(a) = w_k(b) = 0$. Using the method described in Section 2.1.5, the eigenvalue problems in (2.81) can be written on the matrix forms [32]

$$\begin{aligned} \begin{pmatrix} \eta(\kappa)M(\kappa) & M(\kappa) \\ M(\kappa) & -\eta(\kappa)U - A \end{pmatrix} \begin{pmatrix} \Phi_1 \\ \Phi_2 \end{pmatrix} &= \epsilon \begin{pmatrix} M(\kappa) & 0 \\ 0 & U \end{pmatrix} \begin{pmatrix} \Phi_1 \\ \Phi_2 \end{pmatrix}, \\ \begin{pmatrix} \eta(-\kappa)\tilde{M}(\kappa) & \tilde{M}(\kappa) \\ \tilde{M}(\kappa) & -\eta(-\kappa)U - A \end{pmatrix} \begin{pmatrix} \tilde{\Phi}_1 \\ \tilde{\Phi}_2 \end{pmatrix} &= \epsilon \begin{pmatrix} \tilde{M}(\kappa) & 0 \\ 0 & U \end{pmatrix} \begin{pmatrix} \tilde{\Phi}_1 \\ \tilde{\Phi}_2 \end{pmatrix}, \end{aligned} \tag{2.83}$$

where

$$M_{jk}(\kappa) = \left\langle B(\kappa)w_j \middle| B(\kappa)w_k \right\rangle, \quad \tilde{M}_{jk}(\kappa) = \left\langle B^\dagger(-\kappa)w_j \middle| B^\dagger(-\kappa)w_k \right\rangle \tag{2.84}$$

and

$$U_{jk} = \left\langle w_j \middle| w_k \right\rangle, \quad A_{jk} = \left\langle w_j \middle| A \middle| w_k \right\rangle. \tag{2.85}$$

The solutions Φ and $\tilde{\Phi}$ be transformed to solutions ψ of the original Hamiltonian H_0 through the unitary transformation

$$\psi = -\operatorname{sgn}(\epsilon)U^{-1}(\kappa)\Phi, \quad \psi = \operatorname{sgn}(\epsilon)\tilde{U}^{-1}(\kappa)\tilde{\Phi}. \tag{2.86}$$

2.3.3 B-splines

The linearly independent functions w_k that will be used to construct the basis sets in (2.82) for solving the radial Dirac equation are the piecewise polynomials called *B-splines*. For details on these functions, see [33]. The B-splines have finite support, and properties that make them suitable for atomic physics calculations [34].

Cox-de Boor recursion relation

The B-splines are often created using the Cox-de Boor recursion relation, which can be stated as follows [34]. The n_1 first order B-splines defined on the $n_1 + 1$ *knot points* t_i, where $t_i \leq t_{i+1}$, are given by

$$B_i^1(x) = \begin{cases} 1, & t_i \leq x < t_{i+1} \\ 0, & \text{otherwise} \end{cases} . \tag{2.87}$$

The $n_k = n_{k-1} - 1$ B-splines of order k are built recursively from the first order B-splines by the equation

$$B_i^k(x) = \frac{x - t_i}{t_{i+k-1} - t_i} B_i^{k-1}(x) + \frac{t_{i+k} - x}{t_{i+k} - t_{i+1}} B_{i+1}^{k-1}(x). \tag{2.88}$$

As can be deduced from the above recursion relation, the B-splines of order k are only non-zero on the interval $[t_i, t_{i+k}]$, which gives them the finite support. The ordered set of points $t_1 \leq t_2 \leq \ldots \leq t_{n+k}$ is called the *knot vector*. As can be seen from the definition of the B-splines, there is a freedom in the choice of the knot vector; the only demand is that the values of the knot points should be nondecreasing. In this thesis, a convention for the knot vector called the *open uniform* knot vector will be used in the calculations. The open uniform knot vector has k coinciding knot points at each of the end points of the domain, or, in other words

$$\begin{aligned} t_i &= t_1, & i &\leq k \\ t_{i+1} - t_i &= \text{const.}, & k &\leq i \leq n \\ t_i &= t_{k+n}, & i &\geq n + 1. \end{aligned} \tag{2.89}$$

The derivative of a B-spline of order k is given by the recursion relation

$$DB_i^k(x) = \frac{k - 1}{t_{i+k-1} - t_i} B_i^{k-1}(x) - \frac{k - 1}{t_{i+k} - t_{i+1}} B_{i+1}^{k-1}(x). \tag{2.90}$$

We will integrate the products of the B-splines used for making the matrices in (2.83) using the *Gauss-Legendre quadrature*.

Gauss-Legendre quadrature

The following properties of the Gauss-Legendre quadrature are taken from [35, Section 8.5]. The integral of a function $f(x)$ on the interval $x \in [-1, 1]$ can be approximated by the quadrature formula

$$\int_{-1}^{1} f(x)\,\mathrm{d}x = \sum_{i=1}^{n} w_i f(x_i) + E, \tag{2.91}$$

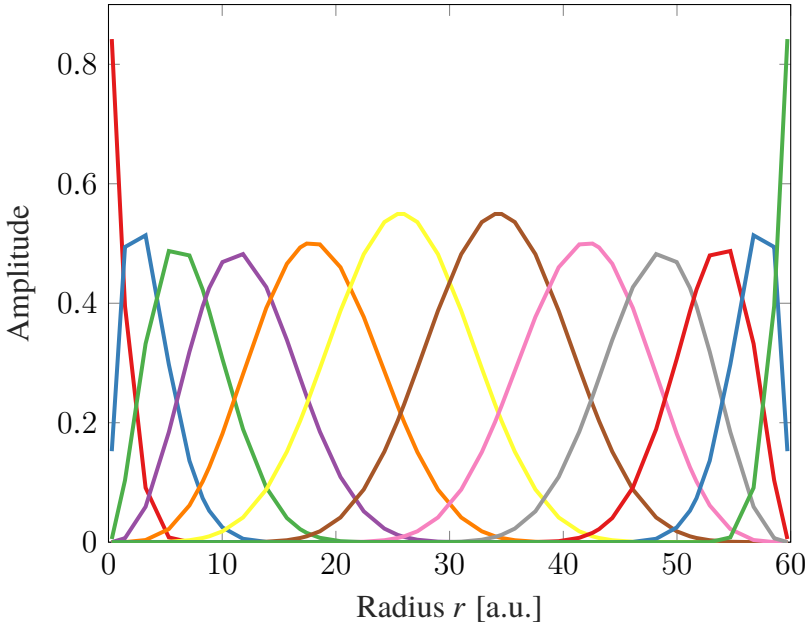

Figure 2.5: 12 B-splines of order 6 defined on Gauss-Legendre points on the domain $r \in [0, 60]$ a.u.

where the *Gauss-Legendre points* x_i are the ith zeros of the nth *Legendre polynomial* $P_n(x)$, and the *Gauss-Legendre weights* w_i are given by the formula

$$w_i = \frac{2(1 - x_i^2)}{(n+1)^2 P_{n+1}(x_i)^2}. \tag{2.92}$$

The error E in (2.91) is given by

$$E = \frac{2^{2n+1}(n!)^4}{(2n+1)[(2n)!]^3} f^{(2n)}(\xi), \tag{2.93}$$

for some ξ. Since the $2n$'th derivative $f^{(2n)}(\xi)$ of a polynomial f of order less than or equal to $2n$ (degree $2n-1$) is zero, a polynomial of order $2n$ will be integrated *exactly* by (2.91).

Since B-splines of order k are polynomials of order k on the intervals $[t_i, t_{i+1}]$, the Gauss-Legendre quadrature of order k integrates the product $B_i B_j$, which is of order $2k$, exactly [34]. When making the matrices for the eigenvalue problems in (2.83), the the maximum order polynomials that should be integrated is $2k$, which means the results should be exact when using k Gauss-Legendre points. k Gauss-Legendre points were therefore used for making and integrating B-splines of order k. The variable of the integral was changed from $[-1, 1]$ to $[t_i, t_{i+1}]$, to be able to integrate over the domain used for the solution. A plot of 12 B-splines of order 6, using the open uniform knot vector convention and 6 Gauss-Legendre points in each knot point interval $[t_i, t_{i+1}]$ is shown in Figure 2.5. The Dirichlet boundary conditions are imposed by removing the first and last B-splines in the set. This is made possible since $B_i(a) = B_i(b) = 0$ for $i = 2, \ldots, n-1$.

2.4 Numerical solution of the interaction with the laser pulse

The goal of this section is to be able to calculate the time dependent effect of an intense laser pulse on the hydrogen-like atom system. The section follows [36] to some extent. The equation that describes the time evolution of the hydrogen-like atom and laser pulse system is

$$i\frac{\partial\Psi(t)}{\partial t} = H(t)\Psi(t), \tag{2.94}$$

where $H(t)$ is the Hamiltonian from (2.37) and $\Psi(t)$ is the state of the system. The time evolution of the system described by this equation can be written formally by the use of the *time-evolution operator* $U(t_1, t_0)$, which evolves the state from $t = t_0$ to $t = t_1$ [36],

$$\Psi(t_1) = U(t_1, t_0)\Psi(t_0) = \mathcal{T}\exp\left[-i\int_{t_0}^{t_1} H(t)\,\mathrm{d}t\right]\Psi(t_0), \tag{2.95}$$

where $\mathcal{T}$ is the *time-ordering operator*. When doing the time propagation numerically, the propagation is usually performed with a series of time steps Δt. If the size of the time steps is chosen to be so small that the variation of the Hamiltonian over the interval $[t, t + \Delta t)$ is negligible, the time-evolution operator can be approximated by the *short-time propagator*

$$U(t + \Delta t, t) \approx \exp[-i\Delta t H(t)], \tag{2.96}$$

which gives

$$\Psi(t + \Delta t) \approx \exp[-i\Delta t H(t)]\Psi(t). \tag{2.97}$$

This short-time propagator can be applied consecutively to propagate the state of the hydrogen-like atom and laser pulse system in steps from $t = t_0$ to $t = t_1$,

$$U(t_1, t_0) \approx U(t_1, t_1 - \Delta t)\ \ldots U(t_0 + 2\Delta t, t_0 + \Delta t)U(t_0 + \Delta t, t_0). \tag{2.98}$$

The Hamiltonian operator in the short-time propagator (2.97) will be treated explicitly by writing it on matrix form. This will be done by expanding $\Psi(t)$ in the finite set of M eigenstates for the hydrogen-like atom ψ_j, with quantum numbers (n_j, κ_j, μ_j), found in Section 2.3. Each eigenstate ψ_j will have the corresponding coefficient $c_j(t)$ in the expansion. Then, using the method in Section 2.1.5, one obtains the Hamiltonian on matrix form,

$$\mathbf{H}(t) = \mathbf{H}_0 + \mathbf{V}(t), \tag{2.99}$$

where the elements of $\mathbf{H}_0$ and $\mathbf{V}(t)$ will be given shortly. The state of the system is then represented by the coefficient vector

$$|\Psi(t)\rangle = \begin{pmatrix} c_1(t) \\ c_2(t) \\ \vdots \\ c_M(t) \end{pmatrix}, \tag{2.100}$$

where each coefficient $c_j(t)$ is related to the hydrogen-like eigenstate ψ_j. The state of the electron in the hydrogen-like system at $t = 0$ is defined through the choice of the

coefficients $c_j(0)$. The Hamiltonian matrix in (2.99) will be used as the Hamiltonian operator and Ψ will be used as the state in the short-time propagator in (2.97), giving

$$|\Psi(t+\Delta t)\rangle \approx \exp[-i\Delta t\mathbf{H}(t)]\,|\Psi(t)\rangle\,. \tag{2.101}$$

More information of how this short-time propagator will be applied at each time step will be given in Section 2.4.2.

Following Section 2.1.5, the elements of the matrix $\mathbf{H_0}$ in (2.99) can be given by

$$(\mathbf{H_0})_{ij} = \langle\psi_i|\,H_0\,|\psi_j\rangle = E_j\delta_{ij}. \tag{2.102}$$

As can be seen, this matrix is a diagonal matrix containing energies of the states found in Section 2.3. A way of calculating the interaction matrix elements $(\mathbf{V}_(t))_{ij}$ for both the dipole and beyond-dipole approximations will be shown in the following section.

2.4.1 Interaction matrix elements

The part of the Hamiltonian describing the interaction with the laser pulse is, from (2.39), given by

$$V(t) = c\boldsymbol{\alpha}\cdot\mathbf{A}(\eta). \tag{2.103}$$

Following Section 2.1.5, the elements of the matrix $\mathbf{V}(t)$ in (2.99) can be given by

$$\begin{aligned}
(\mathbf{V}(t))_{ij} &= \langle\psi_i|\,V(t)\,|\psi_j\rangle \\
&= \langle\psi_i|\,c\boldsymbol{\alpha}\cdot\mathbf{A}(\eta)\,|\psi_j\rangle \\
&= \int\left[\frac{1}{r}\begin{pmatrix}P^*_{n_i,\kappa_i}(r)\chi^\dagger_{\kappa_i,\mu_i}(\hat{\mathbf{r}}) & -iQ^*_{n_i,\kappa_i}(r)\chi^\dagger_{-\kappa_i,\mu_i}(\hat{\mathbf{r}})\end{pmatrix}\begin{pmatrix}0 & cA(\eta)\boldsymbol{\sigma}\cdot\hat{\mathbf{e}}\\ cA(\eta)\boldsymbol{\sigma}\cdot\hat{\mathbf{e}} & 0\end{pmatrix}\right. \\
&\qquad\left.\times\frac{1}{r}\begin{pmatrix}P_{n_j,\kappa_j}(r)\chi_{\kappa_j,\mu_j}(\hat{\mathbf{r}})\\ iQ_{n_j,\kappa_j}(r)\chi_{-\kappa_j,\mu_j}(\hat{\mathbf{r}})\end{pmatrix}\right]\mathrm{d}\mathbf{r} \\
&= ic\int\frac{1}{r^2}P^*_{n_i,\kappa_i}(r)Q_{n_j,\kappa_j}(r)A(\eta)\chi^\dagger_{\kappa_i,\mu_i}(\hat{\mathbf{r}})\boldsymbol{\sigma}\cdot\hat{\mathbf{e}}\chi_{-\kappa_j,\mu_j}(\hat{\mathbf{r}})\,\mathrm{d}\mathbf{r} \\
&\quad - ic\int\frac{1}{r^2}Q^*_{n_i,\kappa_i}(r)P_{n_j,\kappa_j}(r)A(\eta)\chi^\dagger_{-\kappa_i,\mu_i}(\hat{\mathbf{r}})\boldsymbol{\sigma}\cdot\hat{\mathbf{e}}\chi_{\kappa_j,\mu_j}(\hat{\mathbf{r}})\,\mathrm{d}\mathbf{r}\,.
\end{aligned} \tag{2.104}$$

For x-polarized light, where $\hat{\mathbf{e}} = \hat{\mathbf{x}}$, this gives

$$\begin{aligned}
(\mathbf{V}(t))_{ij} =& ic\int\frac{1}{r^2}P^*_{n_i,\kappa_i}(r)Q_{n_j,\kappa_j}(r)A(\eta)\chi^\dagger_{\kappa_i,\mu_i}(\hat{\mathbf{r}})\sigma_x\chi_{-\kappa_j,\mu_j}(\hat{\mathbf{r}})\,\mathrm{d}\mathbf{r} \\
&- ic\int\frac{1}{r^2}Q^*_{n_i,\kappa_i}(r)P_{n_j,\kappa_j}(r)A(\eta)\chi^\dagger_{-\kappa_i,\mu_i}(\hat{\mathbf{r}})\sigma_x\chi_{\kappa_j,\mu_j}(\hat{\mathbf{r}})\,\mathrm{d}\mathbf{r}\,.
\end{aligned} \tag{2.105}$$

Using

$$\chi_{\kappa,\mu}(\hat{\mathbf{r}}) = \begin{pmatrix}\mathrm{sgn}\,(-\kappa)\sqrt{\frac{\kappa+\frac{1}{2}-\mu}{2\kappa+1}}Y_l^{\mu-\frac{1}{2}}(\hat{\mathbf{r}})\\ \sqrt{\frac{\kappa+\frac{1}{2}+\mu}{2\kappa+1}}Y_l^{\mu+\frac{1}{2}}(\hat{\mathbf{r}})\end{pmatrix}, \tag{2.106}$$

and $l = \left|\kappa + \frac{1}{2}\right| - \frac{1}{2}$ from [23], the spherical spinor can be written as

$$\chi_{\kappa,\mu}(\hat{\mathbf{r}}) = \begin{pmatrix} \operatorname{sgn}(-\kappa)\sqrt{\frac{\kappa+\frac{1}{2}-\mu}{2\kappa+1}}\, Y^{\mu-\frac{1}{2}}_{\left|\kappa+\frac{1}{2}\right|-\frac{1}{2}}(\hat{\mathbf{r}}) \\ \sqrt{\frac{\kappa+\frac{1}{2}+\mu}{2\kappa+1}}\, Y^{\mu+\frac{1}{2}}_{\left|\kappa+\frac{1}{2}\right|-\frac{1}{2}}(\hat{\mathbf{r}}) \end{pmatrix}. \tag{2.107}$$

Also, for negative κ,

$$\begin{aligned} \chi_{-\kappa,\mu}(\hat{\mathbf{r}}) &= \begin{pmatrix} \operatorname{sgn}(\kappa)\sqrt{\frac{-\kappa+\frac{1}{2}-\mu}{-2\kappa+1}}\, Y^{\mu-\frac{1}{2}}_{\left|-\kappa+\frac{1}{2}\right|-\frac{1}{2}}(\hat{\mathbf{r}}) \\ \sqrt{\frac{-\kappa+\frac{1}{2}+\mu}{-2\kappa+1}}\, Y^{\mu+\frac{1}{2}}_{\left|-\kappa+\frac{1}{2}\right|-\frac{1}{2}}(\hat{\mathbf{r}}) \end{pmatrix} \\ &= \begin{pmatrix} \operatorname{sgn}(\kappa)\sqrt{\frac{\kappa-\frac{1}{2}+\mu}{2\kappa-1}}\, Y^{\mu-\frac{1}{2}}_{\left|\kappa-\frac{1}{2}\right|-\frac{1}{2}}(\hat{\mathbf{r}}) \\ \sqrt{\frac{\kappa-\frac{1}{2}-\mu}{2\kappa-1}}\, Y^{\mu+\frac{1}{2}}_{\left|\kappa-\frac{1}{2}\right|-\frac{1}{2}}(\hat{\mathbf{r}}) \end{pmatrix}. \end{aligned} \tag{2.108}$$

These identities can be used together with the Pauli matrix in the x-direction

$$\sigma_x = \begin{pmatrix} 0 & 1 \\ 1 & 0 \end{pmatrix}, \tag{2.109}$$

to write

$$\begin{aligned} \chi^{\dagger}_{\kappa_i,\mu_i}(\hat{\mathbf{r}})\sigma_x\chi_{-\kappa_j,\mu_j}(\hat{\mathbf{r}}) &= \operatorname{sgn}(-\kappa_i)\sqrt{\frac{\kappa_i+\frac{1}{2}-\mu_i}{2\kappa_i+1}}\, Y^{\mu_i-\frac{1}{2}}_{\left|\kappa_i+\frac{1}{2}\right|-\frac{1}{2}}{}^{*}(\hat{\mathbf{r}})\sqrt{\frac{\kappa_j-\frac{1}{2}-\mu_j}{2\kappa_j-1}}\, Y^{\mu_j+\frac{1}{2}}_{\left|\kappa_j-\frac{1}{2}\right|-\frac{1}{2}}(\hat{\mathbf{r}}) \\ &\quad + \sqrt{\frac{\kappa_i+\frac{1}{2}+\mu_i}{2\kappa_i+1}}\, Y^{\mu_i+\frac{1}{2}}_{\left|\kappa_i+\frac{1}{2}\right|-\frac{1}{2}}{}^{*}(\hat{\mathbf{r}})\operatorname{sgn}(\kappa_j)\sqrt{\frac{\kappa_j-\frac{1}{2}+\mu_j}{2\kappa_j-1}}\, Y^{\mu_j-\frac{1}{2}}_{\left|\kappa_j-\frac{1}{2}\right|-\frac{1}{2}}(\hat{\mathbf{r}}) \\ &= \operatorname{sgn}(-\kappa_i)\sqrt{\frac{(\kappa_i+\frac{1}{2}-\mu_i)(\kappa_j-\frac{1}{2}-\mu_j)}{(2\kappa_i+1)(2\kappa_j-1)}}\, Y^{\mu_i-\frac{1}{2}}_{\left|\kappa_i+\frac{1}{2}\right|-\frac{1}{2}}{}^{*}(\hat{\mathbf{r}})Y^{\mu_j+\frac{1}{2}}_{\left|\kappa_j-\frac{1}{2}\right|-\frac{1}{2}}(\hat{\mathbf{r}}) \\ &\quad + \operatorname{sgn}(\kappa_j)\sqrt{\frac{(\kappa_i+\frac{1}{2}+\mu_i)(\kappa_j-\frac{1}{2}+\mu_j)}{(2\kappa_i+1)(2\kappa_j-1)}}\, Y^{\mu_i+\frac{1}{2}}_{\left|\kappa_i+\frac{1}{2}\right|-\frac{1}{2}}{}^{*}(\hat{\mathbf{r}})Y^{\mu_j-\frac{1}{2}}_{\left|\kappa_j-\frac{1}{2}\right|-\frac{1}{2}}(\hat{\mathbf{r}}) \end{aligned} \tag{2.110}$$

and

$$\begin{aligned}\chi^{\dagger}_{-\kappa_i,\mu_i}(\hat{\mathbf{r}})\sigma_x\chi_{\kappa_j,\mu_j}(\hat{\mathbf{r}}) &= \operatorname{sgn}(\kappa_i)\sqrt{\frac{\kappa_i-\frac{1}{2}+\mu_i}{2\kappa_i-1}}Y^{\mu_i-\frac{1}{2}}_{|\kappa_i-\frac{1}{2}|-\frac{1}{2}}{}^{*}(\hat{\mathbf{r}})\sqrt{\frac{\kappa_j+\frac{1}{2}+\mu_j}{2\kappa_j+1}}Y^{\mu_j+\frac{1}{2}}_{|\kappa_j+\frac{1}{2}|-\frac{1}{2}}(\hat{\mathbf{r}})\\ &\quad+\sqrt{\frac{\kappa_i-\frac{1}{2}-\mu_i}{2\kappa_i-1}}Y^{\mu_i+\frac{1}{2}}_{|\kappa_i-\frac{1}{2}|-\frac{1}{2}}{}^{*}(\hat{\mathbf{r}})\operatorname{sgn}(-\kappa_j)\sqrt{\frac{\kappa_j+\frac{1}{2}-\mu_j}{2\kappa_j+1}}Y^{\mu_j-\frac{1}{2}}_{|\kappa_j+\frac{1}{2}|-\frac{1}{2}}(\hat{\mathbf{r}})\\ &=\operatorname{sgn}(\kappa_i)\sqrt{\frac{(\kappa_i-\frac{1}{2}+\mu_i)(\kappa_j+\frac{1}{2}+\mu_j)}{(2\kappa_i-1)(2\kappa_j+1)}}Y^{\mu_i-\frac{1}{2}}_{|\kappa_i-\frac{1}{2}|-\frac{1}{2}}{}^{*}(\hat{\mathbf{r}})Y^{\mu_j+\frac{1}{2}}_{|\kappa_j+\frac{1}{2}|-\frac{1}{2}}(\hat{\mathbf{r}})\\ &\quad+\operatorname{sgn}(-\kappa_j)\sqrt{\frac{(\kappa_i-\frac{1}{2}-\mu_i)(\kappa_j+\frac{1}{2}-\mu_j)}{(2\kappa_i-1)(2\kappa_j+1)}}Y^{\mu_i+\frac{1}{2}}_{|\kappa_i-\frac{1}{2}|-\frac{1}{2}}{}^{*}(\hat{\mathbf{r}})Y^{\mu_j-\frac{1}{2}}_{|\kappa_j+\frac{1}{2}|-\frac{1}{2}}(\hat{\mathbf{r}}).\end{aligned} \tag{2.111}$$

Inserting these relations into the interaction term (2.105), we get

$$\begin{aligned}(\mathbf{V}(t))_{ij} &= ic\int\frac{1}{r^2}P^{*}_{n_i,\kappa_i}(r)Q_{n_j,\kappa_j}(r)A(\eta)\\ &\quad\times\left(\operatorname{sgn}(-\kappa_i)\sqrt{\frac{(\kappa_i+\frac{1}{2}-\mu_i)(\kappa_j-\frac{1}{2}-\mu_j)}{(2\kappa_i+1)(2\kappa_j-1)}}Y^{\mu_i-\frac{1}{2}}_{|\kappa_i+\frac{1}{2}|-\frac{1}{2}}{}^{*}(\hat{\mathbf{r}})Y^{\mu_j+\frac{1}{2}}_{|\kappa_j-\frac{1}{2}|-\frac{1}{2}}(\hat{\mathbf{r}})\right.\\ &\quad\left.+\operatorname{sgn}(\kappa_j)\sqrt{\frac{(\kappa_i+\frac{1}{2}+\mu_i)(\kappa_j-\frac{1}{2}+\mu_j)}{(2\kappa_i+1)(2\kappa_j-1)}}Y^{\mu_i+\frac{1}{2}}_{|\kappa_i+\frac{1}{2}|-\frac{1}{2}}{}^{*}(\hat{\mathbf{r}})Y^{\mu_j-\frac{1}{2}}_{|\kappa_j-\frac{1}{2}|-\frac{1}{2}}(\hat{\mathbf{r}})\right)\mathrm{d}\mathbf{r}\\ &\quad-ic\int\frac{1}{r^2}Q^{*}_{n_i,\kappa_i}(r)P_{n_j,\kappa_j}(r)A(\eta)\\ &\quad\times\left(\operatorname{sgn}(\kappa_i)\sqrt{\frac{(\kappa_i-\frac{1}{2}+\mu_i)(\kappa_j+\frac{1}{2}+\mu_j)}{(2\kappa_i-1)(2\kappa_j+1)}}Y^{\mu_i-\frac{1}{2}}_{|\kappa_i-\frac{1}{2}|-\frac{1}{2}}{}^{*}(\hat{\mathbf{r}})Y^{\mu_j+\frac{1}{2}}_{|\kappa_j+\frac{1}{2}|-\frac{1}{2}}(\hat{\mathbf{r}})\right.\\ &\quad\left.+\operatorname{sgn}(-\kappa_j)\sqrt{\frac{(\kappa_i-\frac{1}{2}-\mu_i)(\kappa_j+\frac{1}{2}-\mu_j)}{(2\kappa_i-1)(2\kappa_j+1)}}Y^{\mu_i+\frac{1}{2}}_{|\kappa_i-\frac{1}{2}|-\frac{1}{2}}{}^{*}(\hat{\mathbf{r}})Y^{\mu_j-\frac{1}{2}}_{|\kappa_j+\frac{1}{2}|-\frac{1}{2}}(\hat{\mathbf{r}})\right)\mathrm{d}\mathbf{r}\,.\end{aligned} \tag{2.112}$$

Dipole approximation

If we use the dipole approximation of the vector potential given in (2.72), (2.112) can be written as

$$(\mathbf{V}(t))_{ij} = f(t)(\mathbf{G})_{ij}, \tag{2.113}$$

where

$$f(t) = \frac{E_0}{\omega}\sin^2\left(\frac{\pi t}{T}\right)\sin(\omega t+\phi) \tag{2.114}$$

and

$$
\begin{aligned}
(\mathbf{G})_{ij} =& ic \int P^*_{n_i,\kappa_i}(r) Q_{n_j,\kappa_j}(r)\,\mathrm{d}r\,\delta_{|\kappa_i+\frac{1}{2}|,|\kappa_j-\frac{1}{2}|} \\
&\times \left(\mathrm{sgn}\,(-\kappa_i)\sqrt{\frac{(\kappa_i+\frac{1}{2}-\mu_i)(\kappa_j-\frac{1}{2}-\mu_j)}{(2\kappa_i+1)(2\kappa_j-1)}}\delta_{\mu_i,\mu_j+1} \right. \\
&\left. \quad + \mathrm{sgn}\,(\kappa_j)\sqrt{\frac{(\kappa_i+\frac{1}{2}+\mu_i)(\kappa_j-\frac{1}{2}+\mu_j)}{(2\kappa_i+1)(2\kappa_j-1)}}\delta_{\mu_i,\mu_j-1} \right) \\
&- ic \int Q^*_{n_i,\kappa_i}(r) P_{n_j,\kappa_j}(r)\,\mathrm{d}r\,\delta_{|\kappa_i-\frac{1}{2}|,|\kappa_j+\frac{1}{2}|} \\
&\times \left(\mathrm{sgn}\,(\kappa_i)\sqrt{\frac{(\kappa_i-\frac{1}{2}+\mu_i)(\kappa_j+\frac{1}{2}+\mu_j)}{(2\kappa_i-1)(2\kappa_j+1)}}\delta_{\mu_i,\mu_j+1} \right. \\
&\left. \quad + \mathrm{sgn}\,(-\kappa_j)\sqrt{\frac{(\kappa_i-\frac{1}{2}-\mu_i)(\kappa_j+\frac{1}{2}-\mu_j)}{(2\kappa_i-1)(2\kappa_j+1)}}\delta_{\mu_i,\mu_j-1} \right).
\end{aligned}
\tag{2.115}
$$

The equation (2.115) was implemented in the code, and was used to calculate the stationary part of the dipole approximation interaction matrix.

Beyond dipole approximation

Through repeated use of trigonometric identities, the beyond dipole vector potential component in (2.75) can be written as

$$\begin{aligned}
A(\eta) =& \frac{E_0}{\omega}\sin^2\left(\frac{\pi t}{T}-\frac{\pi z}{cT}\right)\sin(\omega t - kz + \phi) \\
=& \frac{E_0}{\omega}\Bigg[-\frac{1}{4}\sin\left(\omega t + \frac{2\pi t}{T} - kz - \frac{2\pi z}{cT} + \phi\right) \\
&\quad -\frac{1}{4}\sin\left(\omega t - \frac{2\pi t}{T} - kz + \frac{2\pi z}{cT} + \phi\right) \\
&\quad +\frac{1}{2}\sin(\omega t - kz + \phi)\Bigg] \\
=& -\frac{E_0}{4\omega}\sin\left(\omega t + \frac{2\pi t}{T} + \phi\right)\cos\left(kz + \frac{2\pi z}{cT}\right) \\
&+\frac{E_0}{4\omega}\cos\left(\omega t + \frac{2\pi t}{T} + \phi\right)\sin\left(kz + \frac{2\pi z}{cT}\right) \\
&-\frac{E_0}{4\omega}\sin\left(\omega t - \frac{2\pi t}{T} + \phi\right)\cos\left(kz - \frac{2\pi z}{cT}\right) \\
&+\frac{E_0}{4\omega}\cos\left(\omega t - \frac{2\pi t}{T} + \phi\right)\sin\left(kz - \frac{2\pi z}{cT}\right) \\
&+\frac{E_0}{2\omega}\sin(\omega t + \phi)\cos(kz) \\
&-\frac{E_0}{2\omega}\cos(\omega t + \phi)\sin(kz).
\end{aligned} \tag{2.116}$$

This can also be written on a simpler form

$$A(\eta) = \sum_{\alpha=1}^{6} f_\alpha(t) g_\alpha(C_\alpha z), \tag{2.117}$$

where $f_\alpha(t)$ are the time dependent parts of the terms including coefficients, g_α are trigonometric functions (sine or cosine function) and C_α are constants, all of which can be identified from (2.116). Assuming $\omega > \frac{2\pi}{T}$, which is the same as assuming that the length of the envelope is greater than double the wavelength of the carrier, and also assuming that $\phi = 0$, C_α will be strictly positive for all α. We want to expand the space-dependent trigonometric functions in terms of spherical harmonics. Using the spherical harmonic expansion of plane waves [37],

$$e^{i\mathbf{k}\cdot\mathbf{r}} = 4\pi \sum_{l=0}^{\infty}\sum_{m=-l}^{l} i^l j_l(kr) Y_l^{m*}(\hat{\mathbf{k}}) Y_l^m(\hat{\mathbf{r}}), \tag{2.118}$$

and with $\hat{\mathbf{z}}$ being a unit vector in the z-direction [37], we can write

$$\begin{aligned}
\sin(C_\alpha z) =& \frac{1}{2i}\left(e^{iC_\alpha z} - e^{-iC_\alpha z}\right) \\
=& \frac{1}{2i}\left(e^{iC_\alpha r\hat{\mathbf{z}}\cdot\hat{\mathbf{r}}} - e^{-iC_\alpha r\hat{\mathbf{z}}\cdot\hat{\mathbf{r}}}\right) \\
=& \frac{1}{2i}\Bigg(4\pi \sum_{l=0}^{\infty}\sum_{m=-l}^{l} i^l j_l(C_\alpha r) Y_l^{m*}(\hat{\mathbf{z}}) Y_l^m(\hat{\mathbf{r}}) \\
& - 4\pi \sum_{l=0}^{\infty}\sum_{m=-l}^{l} (-i)^l j_l(C_\alpha r) Y_l^{m*}(\hat{\mathbf{z}}) Y_l^m(\hat{\mathbf{r}})\Bigg) \\
=& \, 4\pi \sum_{l=1,3,5,\ldots}^{\infty}\sum_{m=-l}^{l} i^{l-1} j_l(C_\alpha r) Y_l^{m*}(\hat{\mathbf{z}}) Y_l^m(\hat{\mathbf{r}})
\end{aligned} \tag{2.119}$$

and

$$\begin{aligned}
\cos(C_\alpha z) =& \frac{1}{2}\left(e^{iC_\alpha z} + e^{-iC_\alpha z}\right) \\
=& \frac{1}{2}\left(e^{iC_\alpha r\hat{\mathbf{z}}\cdot\hat{\mathbf{r}}} + e^{-iC_\alpha r\hat{\mathbf{z}}\cdot\mathbf{r}}\right) \\
=& \frac{1}{2}\Bigg(4\pi \sum_{l=0}^{\infty}\sum_{m=-l}^{l} i^l j_l(C_\alpha r) Y_l^{m*}(\hat{\mathbf{z}}) Y_l^m(\hat{\mathbf{r}}) \\
& + 4\pi \sum_{l=0}^{\infty}\sum_{m=-l}^{l} (-i)^l j_l(C_\alpha r) Y_l^{m*}(\hat{\mathbf{z}}) Y_l^m(\hat{\mathbf{r}})\Bigg) \\
=& 4\pi \sum_{l=0,2,4,\ldots}^{\infty}\sum_{m=-l}^{l} i^l j_l(C_\alpha r) Y_l^{m*}(\hat{\mathbf{z}}) Y_l^m(\hat{\mathbf{r}}).
\end{aligned} \tag{2.120}$$

From the definition of spherical harmonics commonly used in physics, which is also given in the ISO standard 80000-2:2009 [38], $\theta(\hat{\mathbf{z}}) = 0$. Using the relation [39, Eq. 14.30.4]

$$Y_l^m(0,\varphi) = \begin{cases} \sqrt{\frac{2l+1}{4\pi}}, & m = 0, \\ 0, & m = 1, 2, \ldots, \end{cases} \tag{2.121}$$

the equations (2.119) and (2.120) can be written as

$$\sin(C_\alpha z) = \sum_{l=1,3,5,\ldots}^{\infty} i^{l-1}\sqrt{4\pi(2l+1)}\, j_l(C_\alpha r) Y_l^0(\hat{\mathbf{r}}) \tag{2.122}$$

and

$$\cos(C_\alpha z) = \sum_{l=0,2,4,\ldots}^{\infty} i^{l}\sqrt{4\pi(2l+1)}\, j_l(C_\alpha r) Y_l^0(\hat{\mathbf{r}}). \tag{2.123}$$

Inserting (2.122) and (2.123) into (2.117), we get

$$A(\eta) = \sum_{\alpha=1}^{6} f_\alpha(t) g_\alpha(C_\alpha z), \tag{2.124}$$

where

$$g_\alpha(C_\alpha z) = \begin{cases} \sum_{l=1,3,5,\dots}^{\infty} i^{l-1}\sqrt{4\pi(2l+1)}\, j_l(C_\alpha r) Y_l^0(\hat{\mathbf{r}}), & g_\alpha(C_\alpha z) = \sin(C_\alpha z) \\ \sum_{l=0,2,4,\dots}^{\infty} i^{l}\sqrt{4\pi(2l+1)}\, j_l(C_\alpha r) Y_l^0(\hat{\mathbf{r}}), & g_\alpha(C_\alpha z) = \cos(C_\alpha z). \end{cases} \tag{2.125}$$

Using this relation we can write the interaction term from (2.112) as

$$(\mathbf{V}(t))_{ij} = \sum_{\alpha=1}^{6} f_\alpha(t)(\mathbf{G}_\alpha)_{ij}, \tag{2.126}$$

where

$$(\mathbf{G}_\alpha)_{ij} = \begin{cases} \sum_{l=1,3,5,\dots}^{\infty} \Big[i \int P^*_{n_i,\kappa_i}(r) Q_{n_j,\kappa_j}(r) j_l(C_\alpha r)\,\mathrm{d}r\,(K_{i,j,l} + L_{i,j,l}) \\ \qquad i \int Q^*_{n_i,\kappa_i}(r) P_{n_j,\kappa_j}(r) j_l(C_\alpha r)\,\mathrm{d}r\,(M_{i,j,l} + N_{i,j,l}) \Big], & g_\alpha(C_\alpha z) = \sin(C_\alpha z), \\ \sum_{l=0,2,4,\dots}^{\infty} \Big[- \int P^*_{n_i,\kappa_i}(r) Q_{n_j,\kappa_j}(r) j_l(C_\alpha r)\,\mathrm{d}r\,(K_{i,j,l} + L_{i,j,l}) \\ \qquad - \int Q^*_{n_i,\kappa_i}(r) P_{n_j,\kappa_j}(r) j_l(C_\alpha r)\,\mathrm{d}r\,(M_{i,j,l} + N_{i,j,l}) \Big], & g_\alpha(C_\alpha z) = \cos(C_\alpha z). \end{cases} \tag{2.127}$$

The constants $K_{i,j,l}$, $L_{i,j,l}$, $M_{i,j,l}$ and $N_{i,j,l}$ in (2.127) are given by

$$\begin{aligned} K_{i,j,l} =& c\,\mathrm{sgn}\,(-\kappa_i) i^{l-1} \sqrt{\frac{4\pi(2l+1)(\kappa_i + \frac{1}{2} - \mu_i)(\kappa_j - \frac{1}{2} - \mu_j)}{(2\kappa_i+1)(2\kappa_j-1)}} \\ & \times \int Y^{\mu_i - \frac{1}{2}}_{|\kappa_i + \frac{1}{2}|-\frac{1}{2}}{}^*(\hat{\mathbf{r}}) Y^{\mu_j+\frac{1}{2}}_{|\kappa_j-\frac{1}{2}|-\frac{1}{2}}(\hat{\mathbf{r}}) Y_l^0(\hat{\mathbf{r}})\,\mathrm{d}\hat{\mathbf{r}}, \end{aligned} \tag{2.128}$$

$$\begin{aligned} L_{i,j,l} =& c\,\mathrm{sgn}\,(\kappa_j) i^{l-1} \sqrt{\frac{4\pi(2l+1)(\kappa_i + \frac{1}{2} + \mu_i)(\kappa_j - \frac{1}{2} + \mu_j)}{(2\kappa_i+1)(2\kappa_j-1)}} \\ & \times \int Y^{\mu_i + \frac{1}{2}}_{|\kappa_i + \frac{1}{2}|-\frac{1}{2}}{}^*(\hat{\mathbf{r}}) Y^{\mu_j-\frac{1}{2}}_{|\kappa_j-\frac{1}{2}|-\frac{1}{2}}(\hat{\mathbf{r}}) Y_l^0(\hat{\mathbf{r}})\,\mathrm{d}\hat{\mathbf{r}}, \end{aligned} \tag{2.129}$$

$$\begin{aligned} M_{i,j,l} =& - c\,\mathrm{sgn}\,(\kappa_i) i^{l-1} \sqrt{\frac{4\pi(2l+1)(\kappa_i - \frac{1}{2} + \mu_i)(\kappa_j + \frac{1}{2} + \mu_j)}{(2\kappa_i-1)(2\kappa_j+1)}} \\ & \times \int Y^{\mu_i - \frac{1}{2}}_{|\kappa_i - \frac{1}{2}|-\frac{1}{2}}{}^*(\hat{\mathbf{r}}) Y^{\mu_j+\frac{1}{2}}_{|\kappa_j+\frac{1}{2}|-\frac{1}{2}}(\hat{\mathbf{r}}) Y_l^0(\hat{\mathbf{r}})\,\mathrm{d}\hat{\mathbf{r}}, \end{aligned} \tag{2.130}$$

$$\begin{aligned} N_{i,j,l} =& - c\,\mathrm{sgn}\,(-\kappa_j) i^{l-1} \sqrt{\frac{4\pi(2l+1)(\kappa_i - \frac{1}{2} - \mu)(\kappa_j + \frac{1}{2} - \mu_j)}{(2\kappa_i-1)(2\kappa_j+1)}} \\ & \times \int Y^{\mu_i + \frac{1}{2}}_{|\kappa_i - \frac{1}{2}|-\frac{1}{2}}{}^*(\hat{\mathbf{r}}) Y^{\mu_j-\frac{1}{2}}_{|\kappa_j+\frac{1}{2}|-\frac{1}{2}}(\hat{\mathbf{r}}) Y_l^0(\hat{\mathbf{r}})\,\mathrm{d}\hat{\mathbf{r}}\,. \end{aligned} \tag{2.131}$$

Using a formula for the integral of the triple product of spherical harmonics (the Gaunt integral) [39, Eq. 34.3.22],

$$\int Y_{l_1}^{m_1}(\hat{\mathbf{r}})Y_{l_2}^{m_2}(\hat{\mathbf{r}})Y_{l_3}^{m_3}(\hat{\mathbf{r}})\,\mathrm{d}\hat{\mathbf{r}} = \sqrt{\frac{(2l_1+1)(2l_2+1)(2l_3+1)}{4\pi}}\begin{pmatrix} l_1 & l_2 & l_3 \\ 0 & 0 & 0 \end{pmatrix}\begin{pmatrix} l_1 & l_2 & l_3 \\ m_1 & m_2 & m_3 \end{pmatrix}, \tag{2.132}$$

where the bracket symbols are the Wigner $3j$-symbols, together with the relation [39, Eq. 14.30.6]

$$Y_l^{m*} = (-1)^m Y_l^{-m}, \tag{2.133}$$

we get

$$\begin{aligned}\int Y_{l_1}^{m_1*}(\hat{\mathbf{r}})Y_{l_2}^{m_2}(\hat{\mathbf{r}})Y_{l_3}^{m_3}(\hat{\mathbf{r}})\,\mathrm{d}\hat{\mathbf{r}} =&(-1)^{m_1}\sqrt{\frac{(2l_1+1)(2l_2+1)(2l_3+1)}{4\pi}} \\ &\times\begin{pmatrix} l_1 & l_2 & l_3 \\ 0 & 0 & 0 \end{pmatrix}\begin{pmatrix} l_1 & l_2 & l_3 \\ -m_1 & m_2 & m_3 \end{pmatrix}.\end{aligned} \tag{2.134}$$

A useful property of the Wigner $3j$-symbols are that they have the value of zero unless the following two conditions are satisfied [39, Eq. 34.2.1, Eq. 34.2.3]

$$\begin{aligned} &m_1' + m_2' + m_3' = 0, \\ &\left|l_1' - l_2'\right| \le l_3' \le l_1' + l_2', \end{aligned} \tag{2.135}$$

where the m_i' are the lower and the l_i' are the upper components of the Wigner $3j$-symbols. We can use (2.134) and (2.135) to rewrite (2.128) as

$$\begin{aligned}K_{i,j,l} =&c(-1)^{\mu_i+\frac{l}{2}}(2l+1)\,\mathrm{sgn}\,(\kappa_i)\sqrt{\left|\kappa_i+\frac{1}{2}-\mu_i\right|\left|\kappa_j-\frac{1}{2}-\mu_j\right|} \\ &\times\begin{pmatrix} \left|\kappa_i+\frac{1}{2}\right|-\frac{1}{2} & \left|\kappa_j-\frac{1}{2}\right|-\frac{1}{2} & l \\ 0 & 0 & 0 \end{pmatrix}\begin{pmatrix} \left|\kappa_i+\frac{1}{2}\right|-\frac{1}{2} & \left|\kappa_j-\frac{1}{2}\right|-\frac{1}{2} & l \\ -\mu_i+\frac{1}{2} & \mu_j+\frac{1}{2} & 0 \end{pmatrix},\end{aligned} \tag{2.136}$$

with corresponding selection rules

$$\mu_j = \mu_i - 1, \quad \left|\left|\kappa_i+\frac{1}{2}\right|-\left|\kappa_j-\frac{1}{2}\right|\right| \le l \le \left|\kappa_i+\frac{1}{2}\right|+\left|\kappa_j-\frac{1}{2}\right|-1. \tag{2.137}$$

We do the same with (2.129),

$$\begin{aligned}L_{i,j,l} =&c(-1)^{\mu_i+\frac{l}{2}}(2l+1)\,\mathrm{sgn}\,(\kappa_j)\sqrt{\left|\kappa_i+\frac{1}{2}+\mu_i\right|\left|\kappa_j-\frac{1}{2}+\mu_j\right|} \\ &\times\begin{pmatrix} \left|\kappa_i+\frac{1}{2}\right|-\frac{1}{2} & \left|\kappa_j-\frac{1}{2}\right|-\frac{1}{2} & l \\ 0 & 0 & 0 \end{pmatrix}\begin{pmatrix} \left|\kappa_i+\frac{1}{2}\right|-\frac{1}{2} & \left|\kappa_j-\frac{1}{2}\right|-\frac{1}{2} & l \\ -\mu_i-\frac{1}{2} & \mu_j-\frac{1}{2} & 0 \end{pmatrix},\end{aligned} \tag{2.138}$$

where

$$\mu_j = \mu_i + 1, \quad \left|\left|\kappa_i+\frac{1}{2}\right|-\left|\kappa_j-\frac{1}{2}\right|\right| \le l \le \left|\kappa_i+\frac{1}{2}\right|+\left|\kappa_j-\frac{1}{2}\right|-1, \tag{2.139}$$

with (2.130),

$$\begin{aligned} M_{i,j,l} =& c(-1)^{\mu_i+\frac{l}{2}}(2l+1)\,\mathrm{sgn}\,(\kappa_i)\sqrt{\left|\kappa_i-\frac{1}{2}+\mu_i\right|\left|\kappa_j+\frac{1}{2}+\mu_j\right|} \\ &\times \begin{pmatrix} \left|\kappa_i-\frac{1}{2}\right|-\frac{1}{2} & \left|\kappa_j+\frac{1}{2}\right|-\frac{1}{2} & l \\ 0 & 0 & 0 \end{pmatrix} \begin{pmatrix} \left|\kappa_i-\frac{1}{2}\right|-\frac{1}{2} & \left|\kappa_j+\frac{1}{2}\right|-\frac{1}{2} & l \\ -\mu_i+\frac{1}{2} & \mu_j+\frac{1}{2} & 0 \end{pmatrix}, \end{aligned} \tag{2.140}$$

where

$$\mu_j = \mu_i - 1, \quad \left|\left|\kappa_i-\frac{1}{2}\right|-\left|\kappa_j+\frac{1}{2}\right|\right| \le l \le \left|\kappa_i-\frac{1}{2}\right|+\left|\kappa_j+\frac{1}{2}\right|-1, \tag{2.141}$$

and with (2.131),

$$\begin{aligned} N_{i,j,l} =& c(-1)^{\mu_i+\frac{l}{2}}(2l+1)\,\mathrm{sgn}\,(\kappa_j)\sqrt{\left|\kappa_i-\frac{1}{2}-\mu_i\right|\left|\kappa_j+\frac{1}{2}-\mu_j\right|} \\ &\times \begin{pmatrix} \left|\kappa_i-\frac{1}{2}\right|-\frac{1}{2} & \left|\kappa_j+\frac{1}{2}\right|-\frac{1}{2} & l \\ 0 & 0 & 0 \end{pmatrix} \begin{pmatrix} \left|\kappa_i-\frac{1}{2}\right|-\frac{1}{2} & \left|\kappa_j+\frac{1}{2}\right|-\frac{1}{2} & l \\ -\mu_i-\frac{1}{2} & \mu_j-\frac{1}{2} & 0 \end{pmatrix}, \end{aligned} \tag{2.142}$$

where

$$\mu_j = \mu_i + 1, \quad \left|\left|\kappa_i-\frac{1}{2}\right|-\left|\kappa_j+\frac{1}{2}\right|\right| \le l \le \left|\kappa_i-\frac{1}{2}\right|+\left|\kappa_j+\frac{1}{2}\right|-1. \tag{2.143}$$

In the simplifications done above, we have used the property that $\mu \in \left[-|\kappa|+\frac{1}{2}, |\kappa|-\frac{1}{2}\right]$. The equation (2.127) with the constants $K_{i,j,l}$, $L_{i,j,l}$, $M_{i,j,l}$ and $N_{i,j,l}$ was implemented in the code, and was used to calculate the stationary part of the beyond dipole approximation interaction matrix.

Interaction matrix

Inserting the elements of H_0 from (2.102) and the elements of $\mathbf{V}(t)$ from either (2.113) or (2.126) the total Hamiltonian matrix in (2.99) can be written as

$$\mathbf{H}(t) = \mathbf{H}_0 + \sum_\alpha f_\alpha(t)\mathbf{G}_\alpha. \tag{2.144}$$

This matrix is used in the matrix form of the short-time propagator in (2.101).

2.4.2 Krylov space short-time propagator

This section follows [36] to some extent. The matrix exponentiation in (2.101) can be done through expressing the exponential in a Krylov subspace, which is motivated by the Taylor expansion of the matrix exponential in the matrix form of the short-time propagator in (2.101),

$$\exp[-i\Delta t\mathbf{H}(t)]\,|\Psi(t)\rangle = \sum_{k=1}^{\infty}\frac{(-i\Delta t)^{k-1}}{(k-1)!}[\mathbf{H}(t)]^{k-1}\,|\Psi(t)\rangle\,, \tag{2.145}$$

which can be approximated by truncating the expansion to the order L

$$\exp[-i\Delta t\mathbf{H}(t)]\,|\Psi(t)\rangle \approx \sum_{k=1}^{L} \frac{(-i\Delta t)^{k-1}}{(k-1)!}[\mathbf{H}(t)]^{k-1}\,|\Psi(t)\rangle\,. \tag{2.146}$$

All the terms in this truncated expansion live in the Krylov subspace $\mathcal{K}_L(\mathbf{H}(t), |\Psi(t)\rangle)$ of order L, which is spanned by the images of the vector $|\Psi(t)\rangle$ under the first L powers of $\mathbf{H}(t)$,

$$\mathcal{K}_L(\mathbf{H}(t), |\Psi(t)\rangle) = \text{span}\left\{\,|\Psi(t)\rangle\,,\ \mathbf{H}(t)\,|\Psi(t)\rangle\,,\ \mathbf{H}^2(t)\,|\Psi(t)\rangle\,,\ \ldots,\ [\mathbf{H}(t)]^{L-1}\,|\Psi(t)\rangle\,\right\}. \tag{2.147}$$

In this subspace, a orthonormal set of Krylov subspace basis vectors $\{|\mathbf{q}_k(t)\rangle\}_{k=1}^{L}$ can be created. Then, the short-time propagator can be rewritten as

$$\begin{aligned} |\Psi(t+\Delta t)\rangle &\approx \sum_{k=1}^{L}\sum_{j=1}^{L} |\mathbf{q}_k(t)\rangle\,\langle\mathbf{q}_k(t)|\exp[-i\Delta t\mathbf{H}(t)]\,\big|\mathbf{q}_j(t)\big\rangle\,\big\langle\mathbf{q}_j(t)\big|\,|\Psi(t)\rangle \\ &= \sum_{k=1}^{L} |\mathbf{q}_k(t)\rangle\,b_k(t), \end{aligned} \tag{2.148}$$

where

$$b_k(t) = \sum_{j=1}^{L} \langle\mathbf{q}_k(t)|\exp[-i\Delta t\mathbf{H}(t)]\,\big|\mathbf{q}_j(t)\big\rangle\,\big\langle\mathbf{q}_j(t)\big|\Psi(t)\big\rangle, \quad k\in\{1,\ldots,L\}. \tag{2.149}$$

The above expressions can be simplified by arranging the basis vectors $\{|\mathbf{q}_k(t)\rangle\}_{k=1}^{L}$ as column vectors in a matrix $\mathbf{Q}(t)$, and by creating a matrix $\mathbf{h}(t)$ with the elements

$$(\mathbf{h}(t))_{ij} = \langle\mathbf{q}_k(t)|\exp[-i\Delta t\mathbf{H}(t)]\,\big|\mathbf{q}_j(t)\big\rangle\,. \tag{2.150}$$

Then, if we let the first Krylov vector be

$$|\mathbf{q}_1\rangle = \frac{|\Psi(t)\rangle}{\sqrt{\langle\Psi(t)|\Psi(t)\rangle}}, \tag{2.151}$$

and let it be orthogonal to the rest of the Krylov vectors, the short-time propagator in (2.148) can be simplified to

$$|\Psi(t+\Delta t)\rangle \approx \mathbf{Q}(t)\mathbf{b}_L(t), \tag{2.152}$$

where

$$(\mathbf{b}_L(t))_k = \sqrt{\langle\Psi(t)|\Psi(t)\rangle}\,\exp[-i\Delta t\mathbf{h}(t)]_{k1}. \tag{2.153}$$

Since the matrix $\mathbf{H}(t)$ is Hermitian, the *Lanczos algorithm* can be used to find the matrices $\mathbf{Q}(t)$ and $\mathbf{h}(t)$ at each time step. A thorough survey of the Lanczos algorithm can be found in [40]. The matrix $\mathbf{h}(t)$ from the Lanczos algorithm will be tridiagonal and of dimension L, which makes the exponential $\exp[-i\Delta t\mathbf{h}(t)]$ easy to evaluate, especially for small Krylov space orders L. A pseudocode of the Lanczos algorithm used in this thesis is given in Algorithm 1. To remedy orthogonality losses due to finite precision arithmetic, each Krylov vector is reorthogonalized twice against the previous vectors in the Krylov space. From experience, the Hamiltonian matrix and state vector products are by far the most time-consuming operations in the algorithm, and the time added by reorthogonalizing twice is trivial.

Algorithm 1 pseudocode of Lanczos algortithm with double reorthogonalization, based on [40]. The set of diagonal elements $\{d_k\}$ and off-diagonal elements $\{o_k\}$ constitute the Krylov Hamiltonian matrix $\mathbf{h}$. The matrix $\mathbf{Q}$ with column vectors $|\mathbf{q}_i\rangle$ constitute the matrix $\mathbf{Q}$ in $\mathbf{H} = \mathbf{Q}\mathbf{h}\mathbf{Q}^\dagger$.

$|\mathbf{p}\rangle = |\psi(t)\rangle / \sqrt{\langle\psi(t)|\psi(t)\rangle}$
$|\mathbf{q}_1\rangle = |\mathbf{p}\rangle$
for $k = 1$ **to** L **do**
  $|\mathbf{z}\rangle = \mathbf{H}(t)\,|\mathbf{p}\rangle$
  $d_k = \langle\mathbf{p}|\mathbf{z}\rangle$ {Diagonal element k of $\mathbf{h}(t)$.}
  $|\mathbf{z}\rangle = |\mathbf{z}\rangle - \sum_{i=1}^{k} |\mathbf{q}_i\rangle \langle\mathbf{q}_i|\mathbf{z}\rangle$ {Reorthogonalization.}
  $|\mathbf{z}\rangle = |\mathbf{z}\rangle - \sum_{i=1}^{k} |\mathbf{q}_i\rangle \langle\mathbf{q}_i|\mathbf{z}\rangle$ {Double reorthogonalization.}
  if $k \neq L$ **then**
    $o_k = \sqrt{\langle\mathbf{z}|\mathbf{z}\rangle}$ {Off-diagonal element k of $\mathbf{h}(t)$.}
    $|\mathbf{p}\rangle = |\mathbf{z}\rangle / o_k$
    $|\mathbf{q}_{k+1}\rangle = |\mathbf{p}\rangle$
  end if
end for

2.4.3 Total photoionization probability

After interaction with the laser pulse, the probability that the electron has made a transition to the state with the quantum numbers (n_j, κ_j, μ_j), where n_j is the quantum number indexing the different energy solutions for a given κ on a finite domain, at the time t is given by

$$P_j = \left|c_j(t)\right|^2, \tag{2.154}$$

where the coefficient $c_j(t)$ can be found from the state vector (2.100) after propagating the system to the time t. These probabilities are *additive*; they can be added up to give the total probability of transition to a given set of states. The probability that the electron has made transition to any of the positive pseudocontinuum states can then be given by

$$P_{pos} = \sum_{j \in C} \left|c_j(t)\right|^2, \tag{2.155}$$

where C is the set of j such that $E_{n_j} > c^2$. This numerically calculated probability approximates the probability that the electron has made a transition to the analytical positive continuum (see Section 2.2.3). An electron that has made the transition to the positive continuum after interaction with a laser pulse has been *photoionized* by the pulse. Hence, the probability in (2.155) at time T approximates the *photoionzization probability*. Similarly, the probability that the electron has made a transition to any of the negative pseudocontinuum states can be given by

$$P_{neg} = \sum_{j \in \tilde{C}} \left|c_j(T)\right|^2, \tag{2.156}$$

where $\tilde{C}$ is the set of j such that $E_{n_j} < -c^2$.

2.4.4 Energy differential photoionization probability

The energy differential probability for transition to the state with the quantum numbers (n_j, κ_j, μ_j) at the time t can be given by

$$\frac{dP_j}{dE_{n_j}} = \left|c_j(t)\right|^2 \rho(E_{n_j}), \tag{2.157}$$

where ρ is the density of states, which can be approximated using the formula [34]

$$\rho(E_{n_j}) = \frac{2}{E_{n_j+1} - E_{n_j-1}}, \tag{2.158}$$

where E_{n_j+1} and E_{n_j-1} are the energy levels adjacent to E_{n_j} in the same (κ, μ)-channel. The energy differential probabilities for the different (κ_j, μ_j)-channels can be added up to give the total energy differential transition probability for a given energy. The set of E_j-values are discrete and κ-dependent, so care needs to be taken when adding up the energy differential probabilities. In this thesis, the addition is done by first interpolating the energy differential probabilities on a given energy value grid, before adding up the grid values of the differential probabilities. By the same reasoning as in Section 2.4.3, the energy differential transition probability to all (κ_j, μ_j)-channels in the positive pseudocontinuum approximates the analytic energy differential probability of photoionization. The differential probability of photoionization can also be interpreted as the expected *energy distribution* of photoionized electrons. This energy distribution can be found by doing many independent measurements on the energy of the electron after interaction with the laser pulse, in identically prepared systems.

2.5 Numerical methods

The code for creating the basis set, solving the hydrogen-like atom system, calculating the interaction elements and propagating the hydrogen-like atom and laser pulse system was written in the MATLAB language for this thesis.

In the code, the use of *for*-loops was avoided whenever possible, by writing mathematical equations on matrix and vector form and by using the MATLAB function *mtimes* to calculate matrix and vector products. The code uses the MATLAB function *eig* to solve the eigenvalue problems in (2.83). Both *mtimes* and *eig* use highly optimized numerical libraries which spread the load on multiple threads to reduce the computation time.

The full Hamiltonian matrix $\mathbf{H}(t)$ and the state vector $|\Psi(t)\rangle$ was stored in sparse form (storing only non-zero elements) using the MATLAB *sparse* object. The matrix-vector and matrix-matrix products in the time propagator was done using the *mtimes* function, which exploited the sparsity of the matrix and vector. The evaluation of sparse matrix-vector products with the *mtimes* function does unfortunately not use multithreading. From experience, the sparse vector-matrix products still perform better than full matrix-vector products for our calculations.

The exponentiation $\exp[-i\Delta t\mathbf{h}(t)]$ in the time propagator was done using the MATLAB function *expm*.

Chapter 3

Results and discussion

The code developed for this thesis was used to numerically model the *hydrogen atom*, and its interaction with intense laser pulses. In the following chapter, the results from the model are presented. The code was set to model the hydrogen atom by setting the nuclear charge to $Z = 1$, but other hydrogen-like atoms (ions with one electron) could be modeled just as easily by setting Z to other values. The labeling of the bound states in the model are done with the convention in (2.65), and all energies are given by the energy without the rest energy c^2 of the electron.

3.1 Numerical solution of the hydrogen radial equation

In this section, the results from modeling the hydrogen atom before the interaction with the laser pulse is presented. The modeling was done by solving matrix eigenvalue problems with basis sets containing B-splines of order 6 with an open uniform knot vector. This order was found sufficient since the use of higher order B-splines did not improve the results significantly. First, a comparison between the solutions of the Dirac hydrogen radial equation using the ideal basis set and the dual kinetic balance basis set presented in Section 2.3, is given.

3.1.1 Comparison between ideal basis set and dual kinetic balance

In the early versions of the code for solving the Dirac hydrogen radial equation, the *dual kinetic balance* basis set [31] was used for setting up the matrix eigenvalue problem. In the later versions, it was changed to the *ideal basis set* [32]. The main reason for abandoning the dual kinetic balance basis set was that we always found that some of the states solved using this basis set displayed an odd oscillatory behavior near the boundary of the domain. Depending on which basis functions that was removed when implementing the boundary conditions, this oscillatory behavior could be shifted between different states, but no way of removing the behavior on all the states simultaneously was found. When using the ideal basis set, on the other hand, the oscillatory behavior apparently disappeared on all of the solutions simultaneously.

A comparison of a negative pseudocontinuum state solved with the two different basis sets is shown in Figure 3.1. The oscillatory behavior that occurs when using the dual kinetic balance basis was seemingly more apparent for small domain sizes, so the domain $r \in [0, 30]$ a.u. was chosen. The fact that the oscillation appears at the

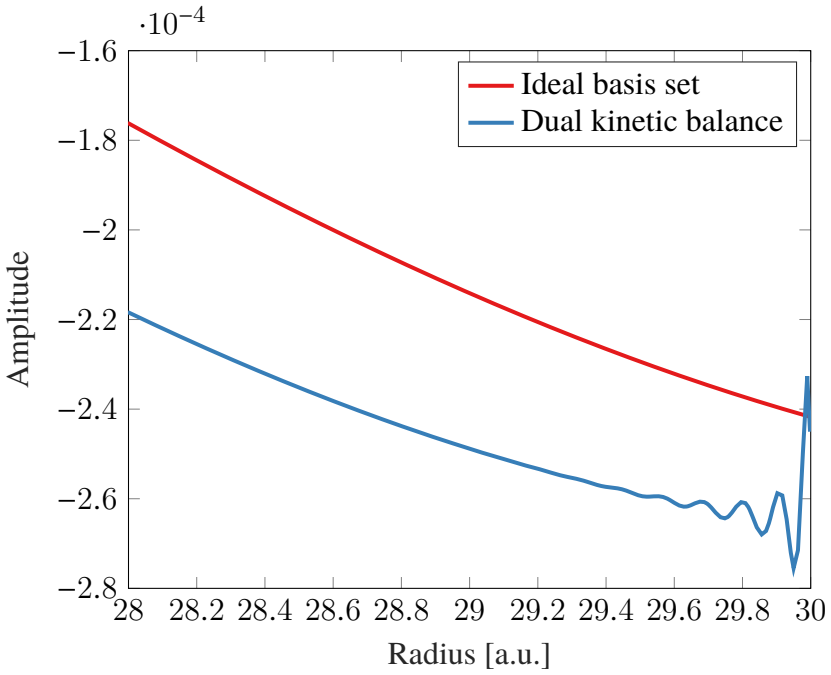

Figure 3.1: The function $P(r)$ of the negative pseudocontinuum state with the highest energy from the solution of the Dirac hydrogen equation with $\kappa = -1$. Shown using both the ideal basis set and the dual kinetic balance basis set. Both basis sets contained 1000 basis functions on the domain $r \in [0, 30]$ a.u. The state is displayed in the interval $r \in [28, 30]$ a.u.

boundary indicates that wrong boundary conditions are imposed when using the dual kinetic balance basis set. For this reason, the ideal basis set was chosen as the basis set for all the solutions in the remainder of this chapter.

3.1.2 Radial probability density and energy of bound states

The ideal basis set was used to solve the Dirac equation for $\kappa = -1$ on the domain $r \in [0, 100]$ a.u. using the method in Section 2.3.2. The radial probability density $r^2\left[|P(r)|^2 + |Q(r)|^2\right]$ can be used for visualizing the shape of the states, and is plotted for the the first five bound states in Figure 3.2. As can be inferred from the figure, the electron has a higher probability for being located close to the nucleus for lower values of the principal quantum number given by (2.66). The energy of these five states is shown in Table 3.1, together with analytical energies from (2.59). As can be seen from the table, the energies from the numerical solutions have a reasonably small difference to the analytical bound state energies, demonstrating that machine precision has been achieved. The $5s_{1/2}$ state, on the other hand, is not well represented in the solution, and is only included to demonstrate that the domain needs to be larger to properly represent bound states with higher principal quantum numbers.

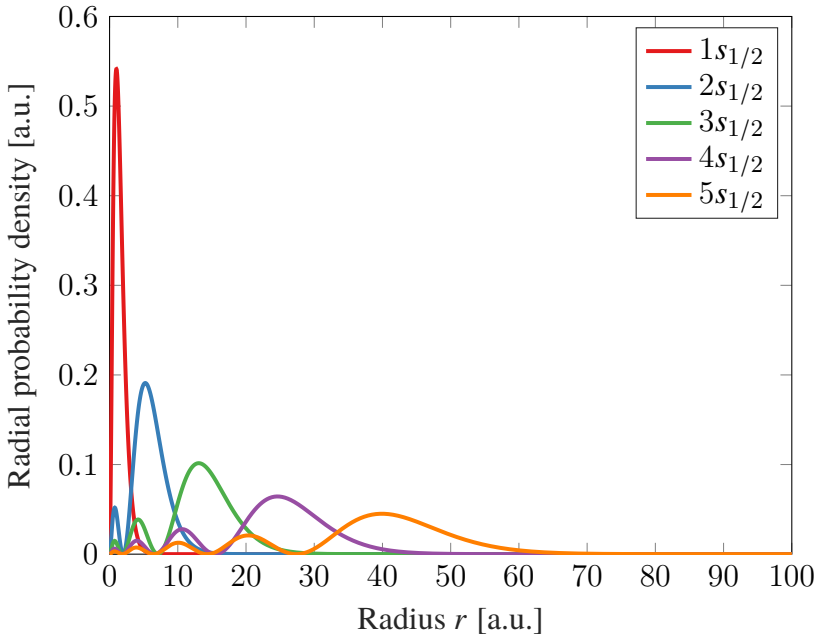

Figure 3.2: The radial probability density of the first five bound states for $\kappa = -1$. Solved using 2000 basis functions on the domain $r \in [0, 100]$ a.u.

Table 3.1: The numerical and analytical energies of the first five bound states of the Dirac equation with $\kappa = -1$. The numerical values are found by using the ideal basis set with 2000 basis functions and $r \in [0, 100]$ a.u. The analytical values are found by using (2.59). The larger difference between the $5s_{1/2}$ numerical and analytic energies is due to the fact that the state is not properly represented on the finite domain used in the solution.

State	Numerical energy [a.u.]	Analytical energy [a.u.]	Absolute energy difference [a.u.]
$1s_{1/2}$	-0.5000066565881	-0.5000066565952	0.0000000000071
$2s_{1/2}$	-0.1250020801890	-0.1250020801894	0.0000000000004
$3s_{1/2}$	-0.0555562951740	-0.0555562951784	0.0000000000044
$4s_{1/2}$	-0.0312503380301	-0.0312503380296	0.0000000000005
$5s_{1/2}$	-0.0200001525664	-0.0200001810578	0.0000000284914

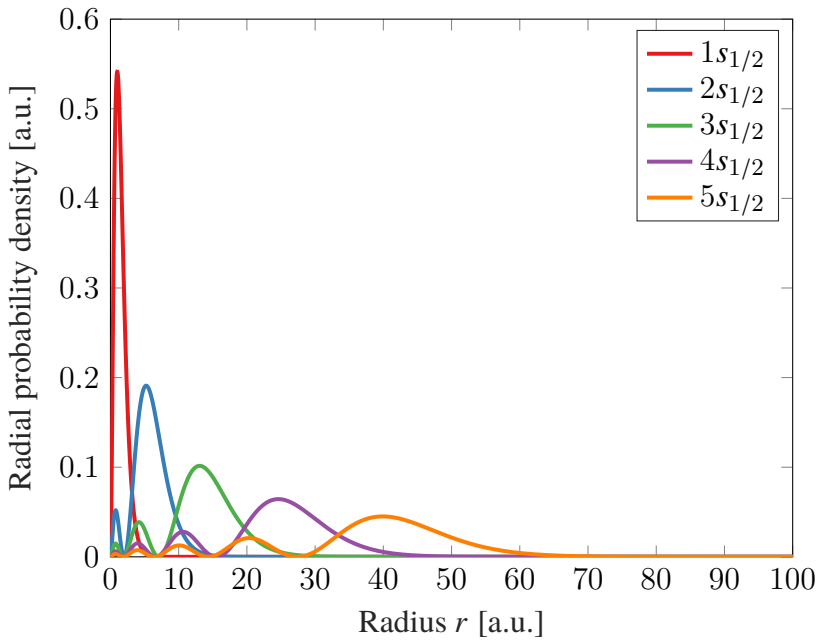

Figure 3.3: The radial probability density of the first five bound states for the Schrödinger equation with $l = 0$. Solved using 2000 basis functions on the domain $r \in [0, 100]$ a.u., with boundary conditions $R(0) = R(100) = 0$.

3.1.3 Difference between Dirac and Schrödinger hydrogen states

To identify relativistic effects in the Dirac equation bound states, they are compared with the Schrödinger equation bound states. The Schrödinger radial equation for hydrogen-like atoms, in atomic units, is given by [20]

$$\left[-\frac{1}{2}\frac{d^2}{dr^2} - \frac{Z}{r} + \frac{l(l+1)}{2r^2} \right] u(r) = Eu(r), \tag{3.1}$$

where $u(r) = rR(r)$. The solution $u(r)$ of radial equation (3.1) was expanded in a finite basis of B-splines of order 6, with an open uniform knot vector, and the matrix eigenvalue problem that comes from using the procedure in Section 2.1.5 was solved. The boundary conditions

$$u(a) = u(b) = 0 \tag{3.2}$$

on the end points a and b of the domain were imposed by removing the first and last B-splines in the set B-splines with an open uniform knot vector. The states are labeled with the principal quantum number N, with the ground state having $N = 1$.

Bound states

The radial probability density $r^2|R(r)|^2$ was used to visualize the shape of the first five bound states from the solution of (3.1) with $l = 0$ and with 2000 basis functions on $r \in [0, 100]$ a.u. The radial probability densities are plotted in Figure 3.3. By comparing this figure to Figure 3.2, it can be seen that the plots of the radial probability density from the Dirac and Schrödinger solutions are virtually indistinguishable. To get a better comparison between the states, the energies of the five first bound states from the Dirac

Table 3.2: The energies of the five first bound states from the Dirac equation for with $\kappa = -1$ and from the Schrödinger equation with $l = 0$. All solutions are done using 2000 basis functions and $r \in [0, 100]$ a.u. The $5s_{1/2}$ is marked in red since the state is not properly represented on the finite domain used in the solution.

State	Dirac energy [a.u.]	Schrödinger energy [a.u.]	Absolute energy difference [a.u.]
$1s_{1/2}$	-0.5000066565881	-0.5000000000000	0.0000066565881
$2s_{1/2}$	-0.1250020801890	-0.1250000000000	0.0000020801890
$3s_{1/2}$	-0.0555562951740	-0.0555555555555	0.0000007396185
$4s_{1/2}$	-0.0312503380301	-0.0312499999996	0.0000003380305
$5s_{1/2}$	-0.0200001525664	-0.0199999715037	0.0000001810627

equation with $\kappa = -1$ and from the Schrödinger equation with $l = 0$ are displayed in Table 3.2. As can be seen from the table, the numerically solved bound state energies from the Dirac equation have a lower value than the Schrödinger ones. The relativistic correction is small; five orders of magnitude smaller than the energies. The ground state is the bound state with the largest correction, and the correction falls off with increasing principal quantum number, given by (2.66). This can be seen in context with the observation made in Section 3.1.2, that the electron has a higher probability for being located close to the nucleus for low principal quantum numbers. The relativistic corrections to the bound states can then be explained by analogy to the behavior of the classical electron: a classical electron bound very close to the nucleus would have centripetal velocities in the regime where relativistic effects would be apparent.

The difference between the Dirac and Schrödinger energies in Table 3.2 are significantly larger than the difference between the numerical and analytical Dirac energies from Table 3.1. Hence, the solution using the ideal basis set and 2000 basis functions gives a good representation of relativistic effects in the bound states.

Pseudocontinuum states

Another question that can be asked is whether relativistic effects occur in the pseudocontinuum states or not. Since the probability densities and energies of the positive pseudocontinuum states are boundary condition dependent, they should not be compared directly when boundary conditions of two solutions are different. The boundary conditions used in the Dirac solution (see Section 2.3.2) are in fact different from the boundary conditions (3.2) used in the Schrödinger equation solution, so a different method of comparing the postive pseudocontinua should be used. A quantity that is independent of the boundary conditions used is the *density of states* in the pseudocontinuum. The density of states for the positive pseudocontinuum states was calculated using (2.158) for both the Dirac and Schrödinger solutions, and plotted in Figure 3.4. As can be seen from the figure, there is a identifiable although small relativistic correction to the density of positive pseudocontinuum states that happens at higher energies; the density of states gets higher when including relativistic effects. This increased density can be explained by a negative relativistic correction to the energies that increases

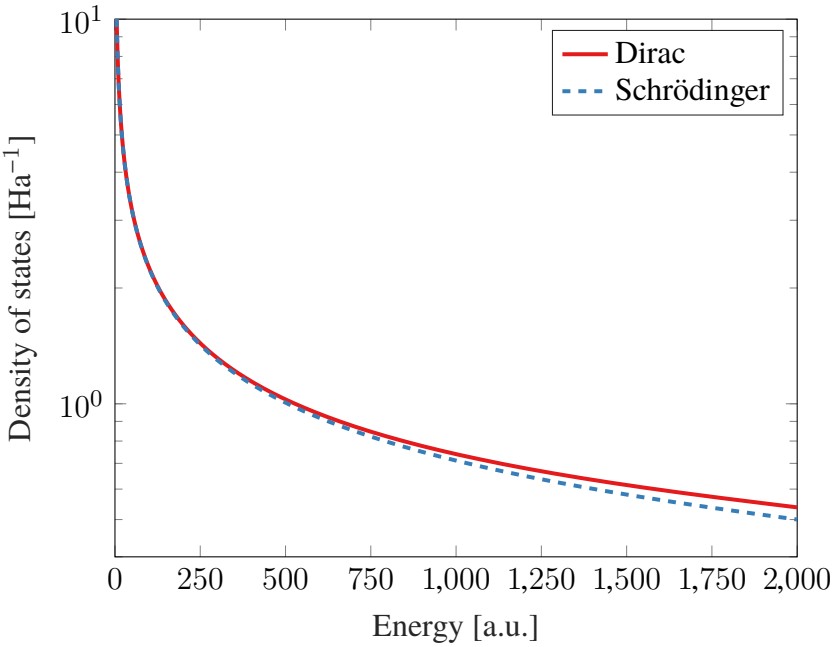

Figure 3.4: The density of the positive pseudocontinuum states for the Dirac and Schrödinger equation solutions. Solved using 6000 basis functions and $\kappa = -1$ for the Dirac equation, and 3000 basis functions and $l = 0$ for the Schrödinger equation. In both solutions, the domain $r \in [0, 100]$ a.u. was used.

for higher energies, effectively condensing the same number of pseudocontinuum states into a smaller energy range. The relativistic correction at higher energies corresponds well with the classical picture: if the energy of a classical electron is high enough, the velocity of the particle is in a regime where relativistic effects would be apparent.

3.2 Numerical solution of the interaction with the laser pulse

In this section, the results from modeling the interactions between the hydrogen atom and intense laser pulses are presented. For the Dirac equation, the solution was done using the method in Section 2.4. In all these Dirac equation solutions, the ideal basis set with B-splines of order 6, with an open uniform knot vector, was used for finding the hydrogen atom eigenstates. The accuracy of the eigenstates is lower for the eigenstates with the highest and lowest energies. Therefore, half of the positive and negative energy states were discarded before propagation. The maximum energies given in this section are the maximum energies after the removal of half of the eigenstates. The propagation was done using 2000 time steps Δt and a Krylov space of dimension $L = 10$, which seemingly gave a negligible error compared to the error caused by the other parameters in the model.

The results from the solution of the Dirac equation will be compared with results from the Schrödinger equation with and without relativistic corrections from [28, 41, 42]. The Hamiltonian operator that is used in these calculations was derived from the Taylor expanded relativistic energy equation in (2.8). If the minimal coupling procedure is

used in (2.8) (see Section 2.2.1), one obtains

$$H = -\frac{Z}{r} + \frac{(\mathbf{p}+\mathbf{A})^2}{2} - \frac{(\mathbf{p}+\mathbf{A})^4}{8c^2} + \dots . \tag{3.3}$$

Inserting the quantum mechanical energy and momentum operators from (2.2) into this equation, and truncating the series, one obtains the Hamiltonian that can be used for finding numerical solutions. When truncating the series at $\frac{(\mathbf{p}+\mathbf{A})^2}{2}$, the nonrelativistic minimally coupled Schrödinger Hamiltonian emerges. The term $\frac{(\mathbf{p}+\mathbf{A})^4}{8c^2}$ will then give the first order relativistic correction to this Hamiltonian. We will refer to this term as the *p^4-correction*. The Hamiltonian in (3.3) does not include spin effects, which are inherent in the Dirac equation. Therefore, hrough the comparison with the results from the Dirac equation, we will be be able to determine whether spin effects play a significant role in the the interactions or not. For more information about spin effects, see a standard textbook on quantum mechanics like [20].

In all the solutions, the electron was prepared in the ground state in the hydrogen atom by setting the coefficient corresponding to the ground state in the state vector (2.100) to 1 at $t = 0$, and the rest of the coefficients to 0. The initial state of the Dirac equation will be chosen to be the state with $n = 0$, $\kappa = -1$ and $\mu = 1/2$, since the two states with $\mu \pm 1$ are degenerate; they both have the same ground state energy. In the Schrödinger equation, the ground state is the state with $N = 1$, $l = 0$ and $m = 0$. In all the calculations, the angular frequency of the carrier in the laser pulse was set to $\omega = 50$ a.u. and the pulse length was set to 15 optical cycles, that is $T = 15\frac{2\pi}{\omega}$ a.u.

3.2.1 Total photoionization probability

The total photoionization probabilities were calculated using (2.155) at time $t = T$, for electric field strengths in the range $E_0 \in [0, 1000]$ a.u. The number of κ-channels that should be included in the eigenstate basis before propagation is, from experience, related to the electric field strength of the laser pulse; higher electric field strengths require more κ-channels for the photoionization probabilities to converge. Therefore, to reduce the computational time needed for calculating all the photoionization probabilities, the number of κ-channels in the eigenstate basis was set to vary with different electric field strengths E_0. The κ-channels used in the solutions, together with the results for the total photoionization probabilities, are shown in Table 3.3. The photoionization probabilities from Table 3.3 is plotted with respect to electric field strength in Figure 3.5. Results from the Schrödinger equation with and without relativistic corrections [41] are also plotted in the figure. In the figure, a notable negative relativistic shift in the photoionization probabilities can be identified for higher electric field strengths E_0. Hence, models describing photoionization at these electric field strengths should preferably incorporate relativistic effects. As can also be seen from the figure, the photoionization probabilities from the Dirac equation correspond well with the probabilities from the p^4-corrected Schrödinger equation for electric field strengths up to $E_0 = 1000$ a.u. This means that corrections due to spin effects and to the higher order terms in (3.3) are small compared to the p^4-correction for all of these electric field strengths. As the electric field strength increases further, one can, from (3.3), expect the p^4-corrected probabilities to also start deviating from the Dirac probabilities. Then, higher orders corrections from (3.3) would

Table 3.3: The total probabilities for photoionization to states with energies below $E = 380$ for the solution of the Dirac equation with different electric field strengths E_0. The maximum energy in the channel with $\kappa = -1$ was $E = 380$ a.u., and the domain used in all the calculations was $r \in [0, 55]$ a.u. The decimals included in the photoionization probabilities are the decimals that match when comparing these results to the ones obtained when only including energies below $E = 330$ a.u.

electric field strength [a.u.]	Range for κ	Photoionization probability
100	$\{-6, \ldots, -1, 1, \ldots, 5\}$	0.00011
200	$\{-7, \ldots, -1, 1, \ldots, 6\}$	0.00043
300	$\{-8, \ldots, -1, 1, \ldots, 7\}$	0.00090
400	$\{-9, \ldots, -1, 1, \ldots, 8\}$	0.00145
500	$\{-10, \ldots, -1, 1, \ldots, 9\}$	0.00202
600	$\{-11, \ldots, -1, 1, \ldots, 10\}$	0.00254
700	$\{-12, \ldots, -1, 1, \ldots, 11\}$	0.00298
800	$\{-13, \ldots, -1, 1, \ldots, 12\}$	0.00335
900	$\{-14, \ldots, -1, 1, \ldots, 13\}$	0.00368
1000	$\{-15, \ldots, -1, 1, \ldots, 14\}$	0.00404

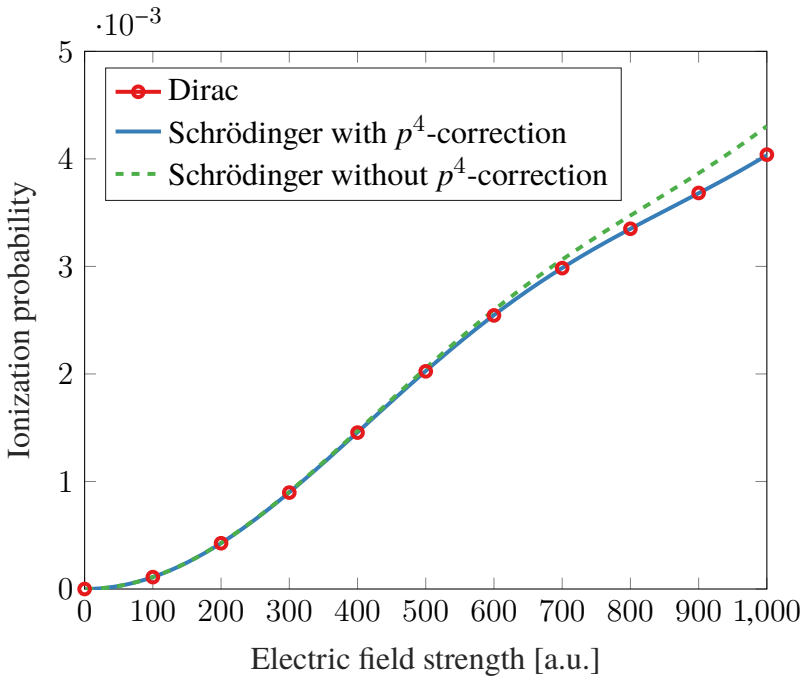

Figure 3.5: The ionization probability plotted with respect to electric field strength for the Dirac equation, and for the Schrödinger equation with and without the p^4-correction [41]. The Dirac equation was solved using κ in Table 3.3, and the Schrödinger equation was solved using $l \in \{0, \ldots, 14\}$. The maximum energy in the channel with $\kappa = -1$ and $l = 0$ was $E = 380$ a.u. The domain used in all the solution was $r \in [0, 55]$ a.u.

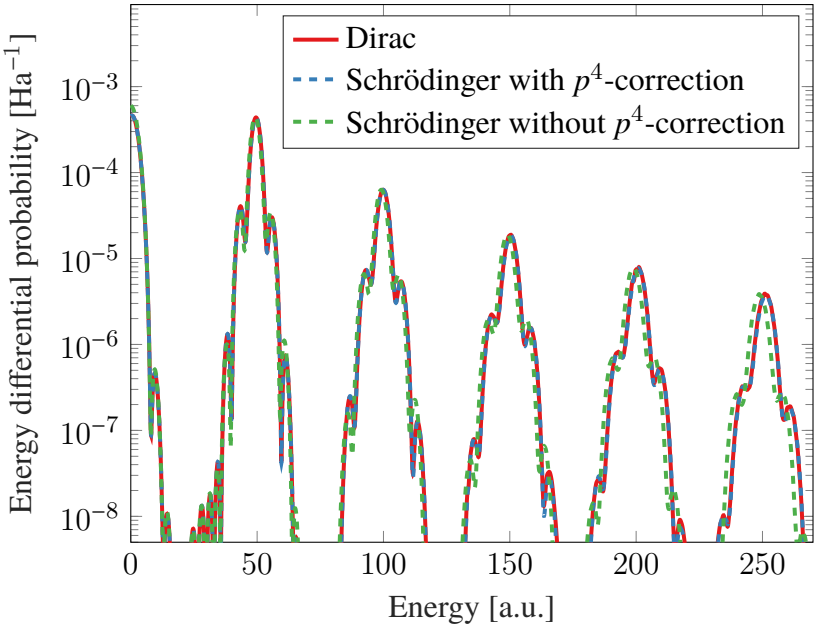

Figure 3.6: The energy differential photoionization probability with the dipole approximation from the Dirac equation with $\kappa \in \{-15, \ldots, -1, 1, \ldots, 14\}$, the Schrödinger equation with relativistic corrections with $l \in \{0, \ldots, 14\}$ [41], and the Schrödinger equation without relativistic corrections with $l \in \{0, \ldots, 14\}$ [41]. The vertical axis of the plot is logarithmic. The electric field strength used was $E_0 = 1000$ a.u., and the maximum energy in the channel with $\kappa = -1$ was $E = 380$ a.u. The domain used in all the solutions was $r \in [0, 55]$ a.u.

have to be incorporated into the Schrödinger equation to keep the good correspondence with the Dirac equation.

3.2.2 Energy differential photoionization probability

The energy differential photoionization probability after interaction with the laser pulse was calculated using (2.157) for different electric field strengths, and for both the dipole and the beyond dipole approximations.

Dipole appoximation

In Figure 3.6, the energy differential photoionization probability with the dipole approximation, for the electric field strength $E_0 = 1000$ a.u., is plotted for the Dirac equation, together with results from the Schrödinger equation with and without the p^4-correction [41]. Compared to the results from the Schrödinger equation without the p^4-correction, the peaks in the differential probability plot are shifted to the right for the results for both the Dirac equation and the Schrödinger results with the p^4-correction. Since the results from the Dirac equation and the Schrödinger equation with the p^4-correction correspond very well, most of the shift can be attributed to the p^4-correction, and not to spin effects or higher order relativistic corrections.

Energy differential photoionization probabilities from the solution of the Dirac equation with the dipole approximation at the electric field strengths $E_0 = 400, 600, 800$ are plotted in Figure 3.7. From the figure, it can be seen that the area under the later

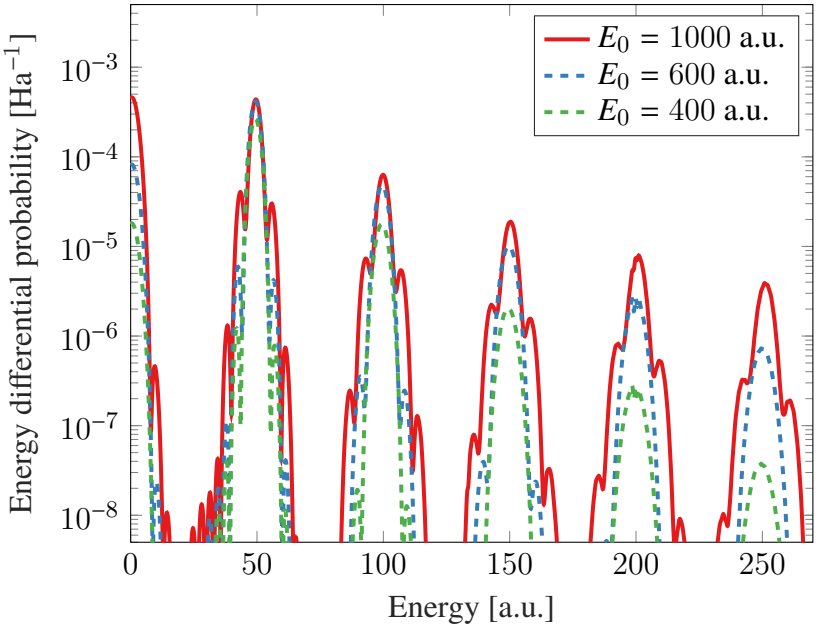

Figure 3.7: The energy differential photoionization probability with the dipole approximation from the Dirac equation at varying electric field strengths E_0. The vertical axis of the plot is logarithmic. The maximum energy in the channel with $\kappa = -1$ was $E = 380$ a.u. after removal of half of the eigenstates. The domain used in all the solutions was $r \in [0, 55]$ a.u.

peaks in the energy differential photoionization probability plot is larger for higher electric field strengths E_0. Hence, the electron has a larger probability of having a higher energy for higher electric field strengths. Since classical electrons with higher energies travel further during the time of propagation, the domain used for the solution should be increased, to not get reflection effects when high energy electrons hit the boundary of the domain.

The later peaks in the photoionization spectrum can be intuitively understood to give the probability of the absorption of several photons (one for each peak). For the absorption of many photons, the electron can do many jumps between (κ, μ)-channels, which justifies the higher number of κ-channels in the the eigenstate basis needed for convergence at higher electric field strengths.

Beyond dipole approximation

In Figure 3.8, the energy differential probabilities for the beyond dipole approximation, for the electric field strength $E_0 = 400$ a.u., was plotted for the Dirac equation, together with results from the Schrödinger equation with both the dipole and beyond dipole approximations. As can be seen from the figure, the magnitude of the energy differential cross section at lower energies differs significantly between the dipole and beyond dipole approximations. The probability for ionization to all positive pseudocontinuum states with energies below $E = 180$ a.u. for the results in Figure 3.8 is $P_{pos} = 0.0027$. The decimals included in this probability are the decimals that match when comparing these results to the ones obtained when only including energies below $E = 130$ a.u. This photoionization probability is almost a factor two larger than the dipole approximation one at $P_{pos} = 0.00145$ from Table 3.3. This factor can be attributed to the large difference

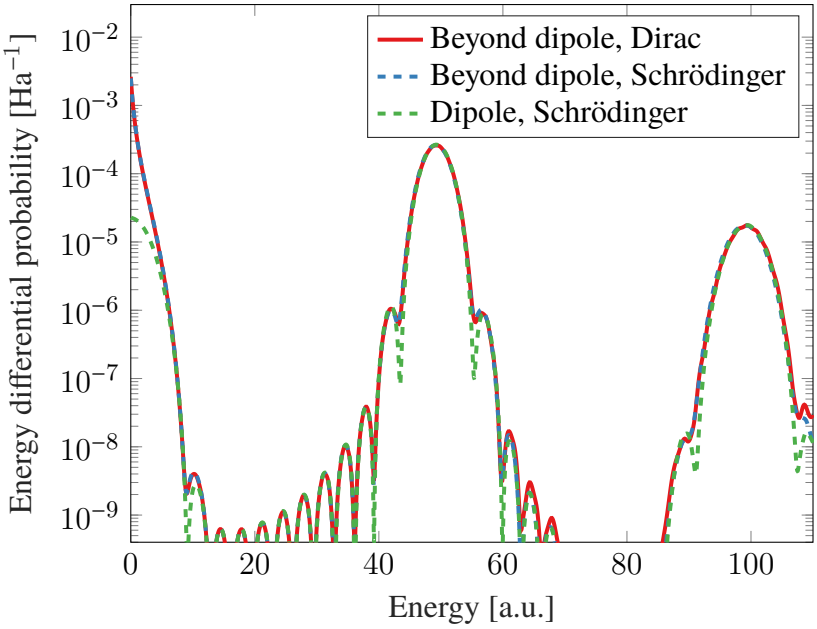

Figure 3.8: The energy differential photoionization probability from the Dirac equation with the beyond dipole approximation $\kappa \in \{-12, \ldots, -1, 1, \ldots, 11\}$, the Schrödinger equation with the beyond dipole approximation [28, 42], and the Schrödinger equation with the dipole approximation [28, 42]. The vertical axis of the plot is logarithmic. The electric field strength used was $E_0 = 400$ a.u. and the maximum energy in the channel with $\kappa = -1$ was $E = 180$ a.u. The domain used in all the solutions was $r \in [0, 30]$ a.u.

in the differential photoionization probabilities at low energies.

The results from the Dirac equation implementation of the beyond dipole approximations coincide well with the results from the Schrödinger equation ones [28, 42] in Figure 3.8. This indicates that the theoretical treatment of the beyond dipole approximation in Section 2.4.1 is valid, and that the approximation has been implemented correctly in the code.

The plot in Figure 3.8 unfortunately only includes two peaks, and the second peak also displays an unwanted oscillatory behavior. Hence, any peak shifts due to the inclusion of relativistic effects in the model is hard to discern, since the shifts can be expected to mainly be visible in the peaks with higher energies, and for higher electric field strengths, see Section 3.2.2. A plot of the first peak of the differential probabilities in 3.8 is displayed in Figure 3.9. As can be seen from the figure, the first peak from the Dirac equation solution with the beyond dipole approximation shows modest signs of being shifted to the right relative to the Schrödinger equation solution with same approximation, but the effect is so small that the existence of the shift should not be concluded from the results. If one wants conclusive results, the maximum available energy and/or electric field strength of the pulse should be increased. The reason for not increasing these parameters in the model was due to limitations in the computational resources that were available for this thesis. The numerical solution of the Dirac equation with the beyond dipole approximation in Figure 3.8 ran for 60 hours on the workstation "IFT040070" at UiB, and used up to 240 GB RAM. Increasing either the size of the domain, the number of basis functions or the number of allowable κ-values (needed for convergence at higher electric field strengths, see Section 3.2.2) increases

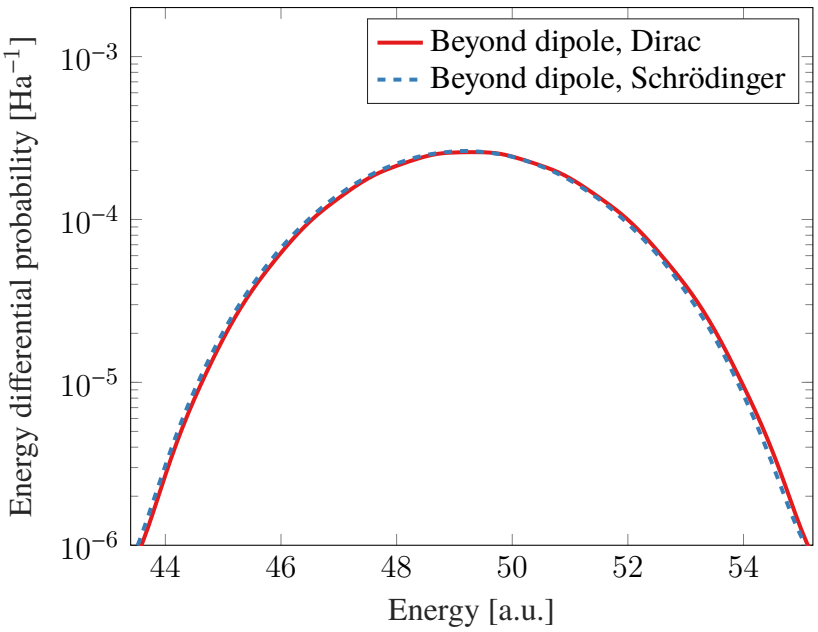

Figure 3.9: The first peak in the energy differential photoionization probability from the Dirac equation with the beyond dipole approximation with $\kappa \in \{-12, \ldots, -1, 1, \ldots, 11\}$, and the Schrödinger equation with the beyond dipole approximation [28, 42]. The vertical axis of the plot is logarithmic. The electric field strength used was $E_0 = 400$ a.u. and the maximum energy in the channel with $\kappa = -1$ was $E = 180$ a.u. The domain used in all the solutions was $r \in [0, 30]$ a.u.

the dimension of the problem substantially. On the machine "IFT040070", which had a total of 251 GB physical RAM available, attempts at increasing the dimensionality made the process crash.

Exclusion of negative energy states in the calculation

A question that has appeared in the literature is whether the negative pseudocontinuum states play a role during the interaction with the laser pulse or not. The inclusion of the negative pseudocontinuum states was found to be important when using a pulse with a carrier angular frequency of 2 a.u., a duration of five optical cycles, and a electric field strength of 30 a.u. [27]. In order to test whether this holds true for the pulse parameters used in this thesis, the Dirac equation was solved with the negative pseudocontinuum states removed before propagating. Otherwise, the solution was done in the same way as the Dirac solution in Figure 3.6. The energy differential photoionization probability with the negative pseudocontinuum removed is plotted in Figure 3.10, together with the result from the regular Dirac solution from Figure 3.6 for comparison. Compared to the regular Dirac equation solution, the peaks in the energy differential photoionization probability plot gets shifted to the left when removing the negative pseudocontinuum states. Hence, we can see that these states have to be included to give a correct solution the Dirac equation. To explain why the negative pseudocontinuum is needed in the solution, the time resolved transition to the positive and negative pseudocontinua were calculated using (2.155) and (2.156), respectively, at each time step. The results are plotted in Figure 3.11. This figure shows that the electron is transmitted to the negative

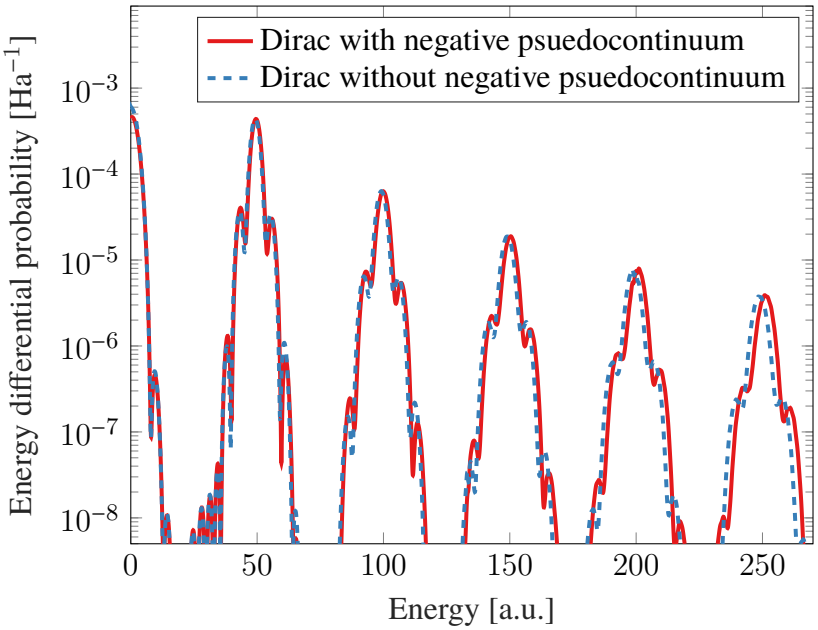

Figure 3.10: The energy differential photoionization probability with the dipole approximation from the Dirac equation with and without negative pseudocontinuum states and $\kappa \in \{-15, , \ldots, -1, 1, \ldots, 14\}$. The vertical axis of the plot is logarithmic. The electric field strength used was $E_0 = 1000$ a.u., and the maximum energy in the channel with $\kappa = -1$ was $E = 380$ a.u. The domain used in the solution was $r \in [0, 55]$ a.u.

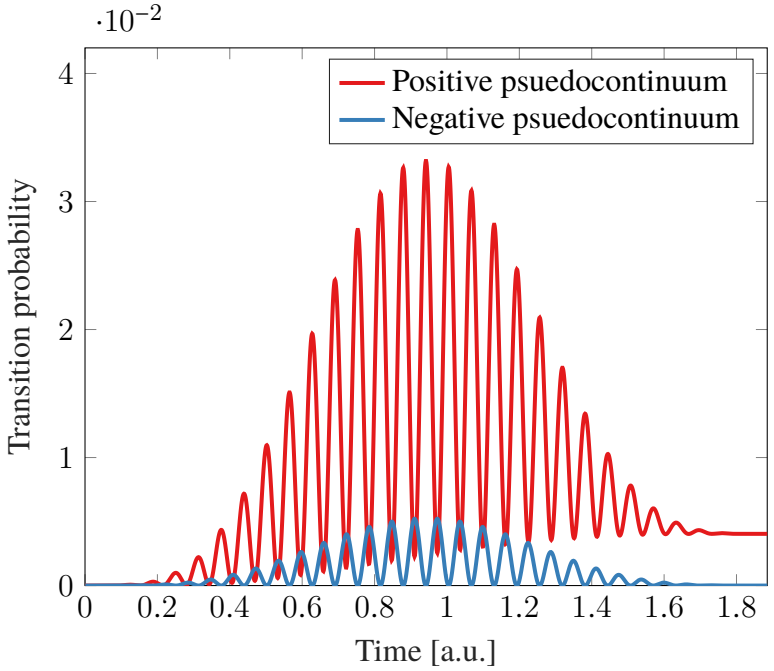

Figure 3.11: The transition probability to the positive and negative pseudocontinua of the Dirac equation for $\kappa \in \{-15, \ldots, -1, 1, \ldots, 14\}$, plotted with respect to time of propagation. The electric field strength used was $E_0 = 1000$ a.u., and the maximum energy in the channel with $\kappa = -1$ was $E = 380$ a.u. The domain used in the solution was $r \in [0, 55]$ a.u.

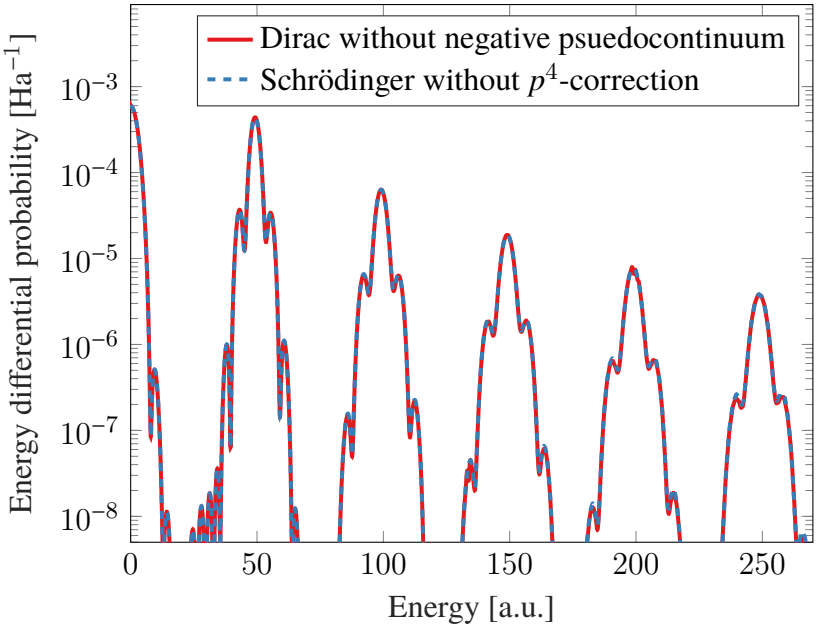

Figure 3.12: The energy differential photoionization probability with the dipole approximation for the Dirac equation without negative pseudocontinuum states $\kappa \in \{-15, \ldots, -1, 1, \ldots, 14\}$, and the Schrödinger equation without relativistic corrections with $l \in \{0, \ldots, 14\}$ [41]. The vertical axis of the plot is logarithmic. The electric field strength used was $E_0 = 1000$ a.u., and the maximum energy in the channel with $\kappa = -1$ was $E = 380$ a.u. The domain used in the solution was $r \in [0, 55]$ a.u.

pseudocontinuum states during the interaction with the laser pulse, but also that the electron leaves the states towards the end of the pulse. This transmission effect is not included when the negative pseudocontinuum states are removed from the solution space prior to propagation, which is the reason for the different results in Figure 3.10.

The energy differential photoionization probability for the Dirac solution without the negative pseudocontinuum states is plotted together with the same result for the nonrelativistic Schrödinger equation in Figure 3.12. As can be seen from the figure, these two results correspond very well. This result can be used to argue that the effect of the relativistic corrections to the field free eigenenergies and eigenstates, that is, relativistic structure effects, play a minor role relative to the corrections due to the inclusion of the negative pseudocontinuum states in the propagation.

Chapter 4

Conclusion and future scope

In this thesis, the Dirac equation for the hydrogen atom before interaction with the laser pulse was solved through the expansion of the solution in both the dual kinetic balance basis set [31] and with the ideal basis set, based on B-splines The solution done with the ideal basis set was chosen since it gave a better behavior at the boundaries of the domain. A small relativistic shift was identified in both the lower energy bound states and higher energy pseudocontinuum states.

The Dirac equation describing the interaction between the hydrogen atom and linearly polarized laser pulses was solved through the use of a short-time propagator with the Lanczos method. A notable relativistic shift in the total photoionization probability and in the locations of the peaks in the peaks in the energy differential probability plot was identified was identified for the dipole approximation. The results corresponded well with result obtained from the Schrödinger equation with p^4-corrections, which implies that spin effects and higher order relativistic corrections play a minor role for the considered pulse parameters. The transmission to the negative pseudocontinuum states was shown to be responsible for almost all of the relativistic effects for high field strengths.

A theoretical treatment of the beyond dipole approximation was developed and implemented, and the results were shown to correspond well with the results from [28, 42]. Since [28] argues that the correction to the dipole approximation photoionization probabilities in the Schrödinger gets large for high field strengths E_0, we can expect the same to happen in the Dirac equation. Hence, the beyond dipole approximation should be used instead of the dipole approximation for higher field strengths. Unfortunately, this requires a much larger eigenstate basis, which increases the computational and memory demands significantly. Therefore, based on the present analysis, we were not able to conclude whether the relativistic shifts observed in the dipole approximation should be present in the actual system.

The main bottleneck of the code developed for this thesis is the sparse matrix-vector products in the Lanczos propagator. The calculation of these products gives high processing and memory demands for a large eigenstate basis. From experience, MATLAB currently (release R2018a) does not use multithreading when calculating these products with the *mtimes* function. Hence, the calculations using the MATLAB code should preferably be run at a computer with high single-core performance (modern CPU infrastructure and high clock speeds).

A more involved way to speed up the calculations would be to use numerical methods

that use multithreading for sparse matrix-vector products, which has been demonstrated in literature [43]. Then, the computation time could be greatly reduced by running the code at high performing computing (HPC) clusters with many CPU cores.

Bibliography

[1] Various 2002 *Early Greek Philosophy (Penguin Classics)* (Penguin Classics) ISBN 0140448152 1.1

[2] Thackray A W 1966 *Isis* **57** 35–55 ISSN 00211753, 15456994 1.1

[3] Bohr N 1913 *The London, Edinburgh, and Dublin Philosophical Magazine and Journal of Science* **26** 1–25 1.1

[4] Schrödinger E 1926 *Phys. Rev.* **28**(6) 1049–1070 1.1

[5] Huygens C 2012 *Treatise on Light (TREDITION CLASSICS)* (tredition) ISBN 9783847201267 1.2

[6] Maxwell J C 1865 *Philosophical transactions of the Royal Society of London* **155** 459–512 1.2

[7] Liu J 2013 *Classical Trajectory Perspective of Atomic Ionization in Strong Laser Fields: Semiclassical Modeling (SpringerBriefs in Physics)* (Springer) ISBN 978-3-642-40549-5 1.3

[8] Freeman R, Bucksbaum P and Mcilrath T 1988 *Quantum Electronics, IEEE Journal of* **24** 1461–1469 ISSN 0018-9197 1.3

[9] Mourou G A, Tajima T and Bulanov S V 2006 *Rev. Mod. Phys.* **78**(2) 309–371 1.3

[10] Einstein A 1905 *Annalen der physik* **322** 891–921 1.3

[11] Dirac P A M 1982 *The Principles of Quantum Mechanics (International Series of Monographs on Physics)* (Clarendon Press) ISBN 0198520115 1.4, 2.1.3

[12] Selstø S, Lindroth E and Bengtsson J 2009 *Physical Review A* **79** 043418 1.4

[13] Kjellsson T, Selstø S and Lindroth E 2017 *Phys. Rev. A* **95**(4) 043403 1.4, 2.2.5

[14] Kjellsson T, Førre M, Simonsen A S, Selstø S and Lindroth E 2017 *Phys. Rev. A* **96**(2) 023426 1.4

[15] Rozenbaum E, Shabaev V M, Sosnova K E and Telnov D A 2014 *Journal of Physics: Conference Series* **488** 032005 1.4

[16] Ruiz D E, Ellison C L and Dodin I Y 2015 *Phys. Rev. A* **92**(6) 062124 1.4

[17] Vanne Y V and Saenz A 2012 *Phys. Rev. A* **85**(3) 033411 1.4

[18] Ivanov I A 2017 *Phys. Rev. A* **96**(1) 013419 1.4

[19] Mohr P J, Newell D B and Taylor B N 2016 *Rev. Mod. Phys.* **88**(3) 035009 1.1, 2.1.1

[20] Griffiths D J 2004 *Introduction to Quantum Mechanics (2nd Edition)* (Pearson Prentice Hall) ISBN 0131118927 2.1.2, 2.2.2, 2.2.4, 3.1.3, 3.2

[21] Grant I P 2006 *Relativistic Quantum Theory of Atoms and Molecules: Theory and Computation (Springer Series on Atomic, Optical, and Plasma Physics)* (Springer) ISBN 0387346716 2.1.2, 2.1.3, 2.2.1, 2.2.2, 2.2.2, 2.2.2, 2.2.2, 2.2.2

[22] Ohlsson T 2012 *Relativistic Quantum Physics: From Advanced Quantum Mechanics to Introductory Quantum Field Theory* (Cambridge University Press) ISBN 1139032682 2.1.3, 2.1.3

[23] Szmytkowski R 2007 *Journal of Mathematical Chemistry* **42** 397–413 ISSN 1572-8897 2.2.2, 2.2.4, 2.2.4, 2.4.1

[24] Villalba V M 1994 *European Journal of Physics* **15** 191 2.2.2

[25] Guseinov I I *International Journal of Quantum Chemistry* **90** 114–118 2.2.2

[26] Dyson F 2011 *Advanced Quantum Mechanics (Second Edition)* (World Scientific Publishing Company) ISBN 9814383414 2.2.3

[27] Selstø S, Lindroth E and Bengtsson J 2009 *Phys. Rev. A* **79**(4) 043418 2.2.5, 3.2.2

[28] Moe T E and Førre M 2018 *Phys. Rev. A* **97**(1) 013415 2.2.5, 2.2.5, 3.2, 3.8, 3.2.2, 3.9, 4

[29] Tupitsyn I I and Shabaev V M 2008 *Optics and Spectroscopy* **105** 183–188 ISSN 1562-6911 2.3.1

[30] Lewin M and Séré É 2014 *Spurious Modes in Dirac Calculations and How to Avoid Them* (Cham: Springer International Publishing) pp 31–52 ISBN 978-3-319-06379-9 2.3.1

[31] Shabaev V M, Tupitsyn I I, Yerokhin V A, Plunien G and Soff G 2004 *Phys. Rev. Lett.* **93**(13) 130405 2.3.1, 3.1.1, 4

[32] Munger C T 2007 *Journal of Mathematical Physics* **48** 022301 2.3.1, 2.3.2, 2.3.2, 3.1.1

[33] de Boor C 2001 *A Practical Guide to Splines (Applied Mathematical Sciences)* (Springer) ISBN 0387953663 2.3.3

[34] Bachau H, Cormier E, Decleva P, Hansen J E and Martín F 2001 *Reports on Progress in Physics* **64** 1815 2.3.3, 2.3.3, 2.3.3, 2.4.4

[35] Hildebrand F B and Mathematics 1987 *Introduction to Numerical Analysis: Second Edition (Dover Books on Mathematics)* (Dover Publications) ISBN 0486653633 2.3.3

[36] Yu C 2017 *Strong-field ionization of two-electron model atoms* Ph.D. Thesis 2.4, 2.4, 2.4.2

[37] Newton R 2013 *Scattering Theory of Waves and Particles (Theoretical and Mathematical Physics)* (Springer) ISBN 3642881300 2.4.1, 2.4.1

[38] 2009 Quantities and units – Part 2: Mathematical signs and symbols to be used in the natural sciences and technology Standard International Organization for Standardization Geneva, CH 2.4.1

[39] *NIST Digital Library of Mathematical Functions* http://dlmf.nist.gov/, Release 1.0.17 of 2017-12-22 f. W. J. Olver, A. B. Olde Daalhuis, D. W. Lozier, B. I. Schneider, R. F. Boisvert, C. W. Clark, B. R. Miller and B. V. Saunders, eds. 2.4.1, 2.4.1, 2.4.1, 2.4.1

[40] Parlett B N 1987 *The Symmetric Eigenvalue Problem (Classics in Applied Mathematics)* (Society for Industrial and Applied Mathematics) ISBN 0898714028 2.4.2, 1

[41] Rossland I K 2018 Private Communication 3.2, 3.2.1, 3.5, 3.6, 3.2.2, 3.12

[42] Førre M 2018 Private Communication 3.2, 3.8, 3.2.2, 3.9, 4

[43] Krotkiewski M and Dabrowski M 2010 *Parallel Computing* **36** 181 – 198 ISSN 0167-8191 4